Modal analysis of in-duct fan broadband noise via an iterative Bayesian inverse approach

A. Pereira, Marc C. Jacob

Modal analysis of in-duct fan broadband noise via an iterative Bayesian inverse approach

A. Pereira[a,*], Marc C. Jacob[a]

[a] *Univ Lyon, École Centrale de Lyon, INSA Lyon, Université Claude Bernard Lyon I, CNRS, Laboratoire de Mécanique des Fluides et d'Acoustique, UMR 5509, Avenue Guy de Collongue, F-69134 Écully Cedex, France*

Abstract

An advanced duct microphone array analysis based on a user friendly iterative Bayesian Inverse Approach (iBIA) has been successfully applied to assess the modal content and the Sound Power Level of fan/outlet guide vanes (OGV) broadband noise. It is shown that iBIA provides considerable reduction of artefacts associated to array sidelobes leading to an improved dynamic range in the reconstructed mode distribution plots. The method also benefits from a data-dependent and fully automated regularisation procedure. Moreover, it allows to control the sparsity degree of the reconstructed modal content: thus different sparsity levels can be tailored for specific noise components, such as fan tones or broadband mode components. It also applies directly to the cross-spectral matrix of measurements, thus advantage can be taken of averaging the data over several snapshots whenever the assumption of stationarity and ergodicity holds. These features facilitate its application to industrially relevant configurations such as the UFFA fan test rig that was operated by AneCom AeroTest in order to deliver reference data for broadband noise modelling in the frame of the European Project TurboNoiseBB. The iBIA has been applied to perform a full azimuthal and radial mode detection as well as axial-wavenumber and azimuthal decompositions. Two configurations of fan/OGV-spacing along two working lines have been tested. The radiated noise has been measured by in-duct microphone arrays located at the intake and downstream of the fan module. Longer rotor-stator gaps are shown to reduce high frequency levels at approach conditions for both inlet and exhaust noise over a large frequency range. The benefit of long gaps tends to vanish for higher fan speeds and even leads to noise increase at high frequencies. Duct sound power estimates obtained from a full azimuthal and radial decomposition have been compared to estimates from both the wavenumber and the azimuthal decompositions, the latter two requiring further assumptions regarding the modal energy distribution. Based on this approach, the widely used equal energy per mode and equal energy density per mode assumptions have thus been evaluated on a large industrially relevant experimental data set.

Keywords: fan broadband noise, mode detection, wavenumber decomposition, inverse methods, Bayesian approach.

1. Introduction

Until the recent Covid-19 crisis, the continuous growth of air traffic combined with an ongoing densification of human habitat in the vicinity of airports was leading to ever more stringent noise emission regulations. A large reduction on the perceived noise emission is an objective of the "Flightpath 2050" recently confirmed by the Advisory Council for Aeronautical Research in Europe (ACARE) [1]. In order to both meet this requirement and reduce fuel consumption, turbofans with increasing bypass ratios have been designed over the years. Currently Utra-High Bypass-Ratio (UHBR) architectures are being developed by engine manufacturers. This trend modifies the relative contribution of individual sound sources on modern aircraft: as a result fan noise contributes to 50%-65% of the overall sound power at certification points (approach, cutback and sideline) [2]. For several reasons, a characteristic feature of modern engines is the increasing broadband contribution to fan noise, which is currently estimated to be

*Corresponding author.
Email addresses: antonio.pereira@ec-lyon.fr (A. Pereira), marc.jacob@ec-lyon.fr (Marc C. Jacob)

about 80 to 90% at approach and 40% at take-off according to ref. [2]. Therefore it is paramount to reduce fan broadband noise, especially during the low altitude approach flight that covers a large area around airports.

A good understanding of noise generation mechanisms is crucial to guide new concepts and noise reduction solutions. Thus, both numerical and experimental approaches are constantly under development to tackle the multiple and highly complex noise sources within a turbofan engine. A frequently used experimental approach, and the one discussed in this paper, is the assessment of the duct modal content by means of acoustic field measurements. Indeed, duct mode propagation is well known and analytically modelled for circular or annular cylinders, but not for complex geometries with more or less rapidly varying diameters, more or less shielded by rotor and/or stator and partly equipped with liners. Experimental mode analysis contributes to source diagnostics as it helps in determining which modes propagate in which frequency range and how. Another important aspect of modal analysis is that it allows for easy computation of the sound power in the duct, which provides good comparison data for CFD-CAA computations. Many unsteady broadband noise computations use free-field analogies (e.g. Ffowcs Williams Hawkings) or annular cylinder-based ones (see Goldstein). A comparison against an experimentally obtained sound power may be very useful if the latter analogy is used.

The experimental assessment of duct modal content has been of interest since the 1960s [3]. At that time, Mugridge [3] used a space/time correlation technique with the data from two traversable hot-wire anemometers by measuring the axial component of the acoustic particle velocity. The use of a microphone couple instead of hot-wires was then investigated by using techniques based on cross-spectral quantities [4, 5]. These approaches consisted either in optimising a series of microphone-couple positions and solving a linear system of equations such as the work by Bolleter and Crocker [4] or in using a fixed microphone while the second one is continuously traversed either along the circumferential or the axial direction, see the work of Harel and Perulli [5]. Pickett *et al.* [6] later proposed a technique using about 10 wall flush-mounted microphones, the positions of which were optimised through a dedicated procedure. Modal amplitudes are estimated by solving a linear system of equations through a matrix inversion. The use of more than two traversing microphones or microphone rakes was investigated by several researchers, either using sequential measurements, see Moore [7], Enghardt *et al.* [8], or using continuously rotating systems, see Heidelberg and Hall [9, 10], Sutliff [11] and Sijtsma and Orsi [12]. Approaches based on static measurements at successive positions have been limited to applications at the Blade Passing Frequency (BPF) and its harmonics, due to the need of a phase reference to synchronise sequential measurements. Extensions for the analysis of fan broadband noise have been investigated by Enghardt *et al.* [13] and Pereira *et al.* [14]. However, these approaches require a relatively large number of array positions as well as several fixed reference probes. Another strategy is to use a large number of fixed wall flush-mounted microphones distributed along the duct circumference and/or duct axis. More details are found in the literature, see Joppa [15, 16] for an example of both circumferential and axial arrays, Sarin and Rademaker [17] for an example of in-flight tests using circumferential rings or Rademaker *et al.* [18] for an optimisation procedure of microphone locations in a ring. Among these works different methods for estimating the modal amplitudes were tested, for instance, simple spatial Fourier transforms over either the circumferential [15, 17, 18] or axial directions [15] or a least squares fit between mode amplitudes and measured acoustic pressure [17]. A more advanced approach using an iterative thresholding algorithm was also proposed by Blacodon [19] for the study of turbine noise in applications for which the signal-to-noise ratio is very poor. The use of array preprocessing methods such as the Principal Component Analysis (PCA) or the cross-correlation with a reference probe was also proposed by Sijtsma and Zillmann [20] to deal with tonal engine exhaust noise using either in-duct or far-field microphones. A technique based on the transfer functions between a set of microphones and a reference microphone proposed by Åbom [21] was used to decompose a broadband in-duct sound field into its different mode components. Measurements on at least two axial sections are carried out to decompose higher order modes into both upstream and downstream propagating modes. This technique was later extended by Sack *et al.* [22] by optimising the microphone locations using a genetic algorithm such as to keep the condition number of the modal matrix small.

Indeed, the use of external microphone arrays for mode detection purposes has also been under investigation over two decades [23, 24, 25, 26, 27, 28]. The use of a fixed polar microphone array centred at the fan inlet combined with a method based on the Polar Correlation Technique was investigated in the late 1970s [23, 24]. Since the early 1990s, some authors proposed using an external circular hoop array vertically centred at the fan inlet and axially traversed along the duct axis [25, 26, 27, 28]. An alternative strategy was to take advantage of the structure supporting the Turbulence Control Screen (TCS) for mounting the microphones. Lan et al. [29] have presented a setup with 40 electret microphones installed on the TCS for the modal detection at the BPF and its harmonics. A duct propagation

code was used to model the transfer function between mode amplitudes and far-field pressure. A classic beamforming approach was then used for the estimation of modal amplitudes. Lewy [30, 31] also proposed a method to estimate mode amplitudes based on free-field directivity measurements. The propagation between modes and far-field sound pressure level is analytically modelled through a Rayleigh integral. No phase information between acoustic pressure is required. An iterative least squares fitting is applied to regularise the problem and enforce mode amplitudes to be positive. Venditti *et al.* [32] have also investigated the problem and proposed two mode identification methods, one based on inter-mode phase elimination and the other based on a least squares minimisation with non-negativity constraints. Castres *et al.* [33, 34, 35] developed a mode detection method for broadband fan noise based on near-field measurements of the acoustic pressure. In their method, amplitudes of both azimuthal and radial modes are estimated by solving an inverse method relating the mode amplitudes to measured pressure data. A regularisation approach is proposed to deal with modes that are very close to their cut-off frequency.

Recent developments in the field of array signal processing techniques resorted to more advanced methods for mode detection purposes. Examples of such are, for instance, deconvolution approaches [36, 37], regularised inverse problems [38, 39], minimisation under sparsity constraints [40, 41, 42] or the use of neural networks [42, 43]. Suzuki and Day [39] compared different methods for the estimation of mode amplitudes of both tonal and broadband noise generated by a loudspeaker array within a rectangular cross-section duct. The comparison included conventional beamforming, CLEAN, matrix pseudo-inverse and generalised-inverse beamforming. Sijtsma and Brouwer [37] applied deconvolution approaches for estimating the azimuthal mode content of both tonal and broadband fan noise. Different approaches were tailored to broadband and tone noise components. For the broadband component the classic deconvolution problem [44] is solved by a non-negative least squares (NNLS) solver. For the tonal component a Matching Pursuit Algorithm is applied by exploiting the sparsity of azimuthal modes. Fauqueux and Davy [36] used a deconvolution approach to estimate both azimuthal and radial mode amplitudes. The problem was formulated in terms of the cross-spectral matrix of measurements. Two assumptions regarding the inter-modal correlation were tested, one assuming the modes to be uncorrelated and one assuming them to be correlated. Behn *et al.* [40] applied ideas from the Compressive Sensing Framework to estimate azimuthal mode amplitudes for tone noise generated by rotor-stator interactions. In their approach, the estimate is obtained in two-steps, first a ℓ_1 minimisation problem is solved by an Orthogonal Matching Pursuit (OMP) Algorithm and a least-squares fit or a Discrete Fourier Transform (DFT) is then applied in a second step to the residual pressure. The residual pressure is obtained by subtracting the pressure reconstructed by the OMP of the total measured pressure. Bu *et al.* [41] also applied a Compressive Sensing scheme to the estimation of azimuthal mode amplitudes. The approach therein differs from that by Behn *et al.* [40] since it proposes firstly to reconstruct the spatial pressure field along the duct circumference and then to apply a classic azimuthal DFT. The spatial pressure field is obtained by solving a ℓ_1 minimisation problem using the CVX toolbox [45] for convex programming. The use of machine learning based techniques has been recently proposed with the aim to cope with more realistic geometries, flow conditions and propagation effects. This has been tested by Huang [42] for spinning mode detection and by Sack et Åbom [43] for the decomposition of plane waves into upstream and downstream propagating modes.

In the present work we propose to use an iterative Bayesian Inverse Approach (iBIA) to solve the mode detection problem. It offers a few advantages that are worth mentioning: the regularisation procedure is fully automated and estimated from the data; it applies equally well for both correlated and uncorrelated noise fields; a parameter can be tuned to allow for the control of the sparsity degree of reconstructed mode distributions making it well suited for both tonal and broadband fan noise. Finally, the method applies directly to the cross-spectral matrix of measurements.

The proposed approach has been applied to data measured within an extensive experimental campaign aimed at characterising fan broadband noise and producing reference data for noise predictions. This campaign was carried out in the framework of the TurboNoiseBB European Project. The azimuthal modal content of broadband noise has been assessed both at the intake and the exhaust duct. In addition the noise at the exhaust duct has been decomposed into wavenumber components thanks to a linear phased array. This work allowed comparing the noise generated by two configurations based on different machine geometries. Finally, an estimate of the duct sound power through a complete decomposition (azimuthal and radial modes) has been compared to estimates based on azimuthal-only and wavenumber decompositions.

The remainder of the manuscript is organised as follows. Section 2 presents an outline of the theory of the in-duct mode detection problem and an overview of iBIA. Section 3 introduces the experimental campaign and highlights the configuration of the microphone arrays. Section 4 summarises and discusses the main results.

2. Outline of theory

This section is organised into three main parts. In the first part a description of the in-duct pressure field using a modal approach is detailed. In the second part, the mode detection problem is formulated using a matrix notation, whereas, in the last three subsections, the method used to solve the mode detection problem is described.

2.1. Modal description of in-duct pressure field

By assuming linear acoustics behaviour and a stationary sound field, the complex acoustic pressure $\hat{p}(z, r, \phi)$ inside a hard-wall cylindrical duct with circular or annular cross-section can be conveniently decomposed into a weighted sum of modes [46]:

$$\hat{p}(z, r, \phi) = \sum_{m=-\infty}^{\infty} \sum_{n=0}^{\infty} \left[A^{+}_{m,n} \mathrm{e}^{\mathrm{j}k^{+}_{z_{m,n}} z} + A^{-}_{m,n} \mathrm{e}^{\mathrm{j}k^{-}_{z_{m,n}} z} \right] f_{m,n}(r) \mathrm{e}^{\mathrm{j}m\phi}, \tag{1}$$

with $A^{+}_{m,n}$ and $A^{-}_{m,n}$ the complex-valued coefficients of modes propagating downstream and upstream respectively. The subscripts m and n are the azimuthal and radial mode orders. Note that an $\mathrm{e}^{-\mathrm{j}\omega t}$ time convention is used. The terms $k^{\pm}_{z_{m,n}}$ are the axial wavenumbers in both downstream ($^{+}$) and upstream ($^{-}$) directions and $f_{m,n}(r)$ is a normalised modal shape factor which depends on the duct's cross section and radial boundary conditions. Expressions of the modal shape factor for both circular and annular duct sections are given in Appendix A. Mode axial wavenumbers $k^{\pm}_{z_{m,n}}$ are in turn given by

$$k^{\pm}_{z_{m,n}} = \frac{1}{\beta^2} \left(-M_z k_0 \pm \hat{k}_{r_{m,n}} \right), \tag{2}$$

where $M_z = U_0/c$ is the Mach number along the z direction, $\beta^2 = 1 - M_z^2$ the squared Prandtl–Glauert factor and $k_0 = \omega/c$ the acoustic wave number. The term $\hat{k}_{r_{m,n}}$ is thus written

$$\hat{k}_{r_{m,n}} = \sqrt{k_0^2 - \beta^2 k^2_{r_{m,n}}}, \tag{3}$$

where $k_{r_{m,n}}$ is a radial (or transversal) wavenumber with values depending on the boundary conditions at the duct walls, i.e. at $r = r_h$ and $r = r_t$ (see Figure 1). The computation of $k_{r_{m,n}}$ is detailed in Appendix A for both annular

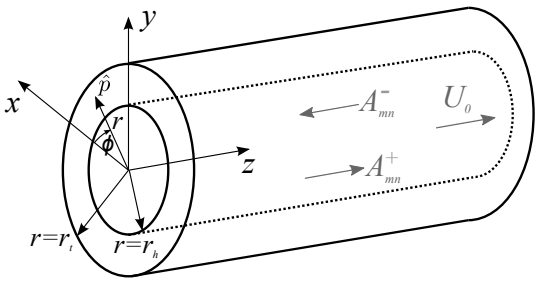

Figure 1: Sketch of the cylindrical coordinate system used in the problem.

and circular duct's cross-section. Modelling the in-duct acoustic pressure through Eq. (1) requires the knowledge of physical quantities such as the mean flow velocity and sound speed that in turn depends on the temperature. From an experimental point of view, these values must be accurately measured to ensure an accurate model of the pressure field. Reductions of Eq. (1) are an interesting approach to avoid this requirement while leading to valuable information. For instance, by setting

$$C_m(z_0, r_0) = \sum_{n=0}^{\infty} \left[A^{+}_{m,n} \mathrm{e}^{\mathrm{j}k^{+}_{z_{m,n}} z} + A^{-}_{m,n} \mathrm{e}^{\mathrm{j}k^{-}_{z_{m,n}} z} \right] f_{m,n}(r), \tag{4}$$

Eq. (1) can be written as

$$\hat{p}(z_0, r_0, \phi) = \hat{p}(\phi) = \sum_{m=-\infty}^{\infty} C_m(z_0, r_0) \mathrm{e}^{\mathrm{j}m\phi}, \tag{5}$$

that decomposes a circumferential pressure field onto a basis of azimuthal modes with coefficients $C_m(z_0, r_0)$. This is indeed the Fourier series of the complex pressure $\hat{p}$ (at a fixed frequency ω) along the azimuthal coordinate ϕ, which is cyclic with period 2π. Note that these coefficients represent the sum over radial orders n, see Eq. (4). Thus, the contribution of both downstream $A^+_{m,n}$ and upstream $A^-_{m,n}$ modes is intrinsically condensed in $C_m(z_0, r_0)$. This is indeed a major limitation of this simplification, since the contribution of both downstream and upstream propagating modes cannot be separated. The dependence of C_m on (z_0, r_0) has been made explicit to emphasize that this decomposition must be carried out at constant axial and radial positions in the duct. This can be achieved for instance, with a ring of acoustic pressure probes. It emphasizes the spinning mode structure of ducted waves. The infinite sum in Eq. (5) must be truncated for practical reasons up to an azimuthal order M that is given by the discretisation of the azimuthal coordinate in the experimental set-up. Another simplified formulation of very practical interest is allowed by a spatial Fourier decomposition of the complex wall pressure fluctuations along the axial coordinate z, as previous work carried by Joppa [15, 16]. This is written as

$$\hat{p}(z) = \int_{-\infty}^{\infty} D_{k_z}(r_0, \phi_0) \mathrm{e}^{\mathrm{j}k_z z} dk_z, \tag{6}$$

that gives the complex pressure $\hat{p}(z) = \hat{p}(z, r_0, \phi_0)$ as a continuous distribution of axial wavenumber components k_z whose coefficients are given by D_{k_z}, and r_0 and ϕ_0 are fixed radial and azimuthal coordinates. This representation emphasizes the axial wave nature of the in-duct sound, propagative waves for real values of wavenumbers k_z (cut-on modes) and damped waves for imaginary wavenumbers k_z (cut-off modes). It is important to note that Eq. (6) does not follow from a direct simplification of Eq. (1), as is the case for Eq. (5). It should be understood as another representation that decomposes the wall-pressure fluctuations measured along the axial coordinate into a continuous distribution of energy with wavenumber. As opposed to the mode axial wavenumbers $k_{z_{m,n}}$ that take only discrete values for individual modes of order (m, n), the k_z in Eq. (6) takes on continuous values. Indeed, at given frequency, the dispersion relation implies that for each azimuthal and radial mode only 2 axial wave numbers are possible: $k^+_{z_{m,n}}$ and $k^-_{z_{m,n}}$. In that perspective, the axial wavenumbers are not continuously distributed. In Eq. (6), the complex pressure at fixed frequency is decomposed into a continuous sum of axial wave components. This is justified by two reasons: the first is that the number of cut-on modes (and accordingly the associated mode density) quickly grows with frequency, thus at frequencies that are not too small, the distribution appears to be almost continuous. As a result, the axial wavenumber can be approximated by a continuous variable. Another reason might be due to axial variations of the duct's cross-section resulting in variations of the axial wavenumber along the z-direction. In practice, due to the limited spatial sampling of linear arrays, aliasing will occur and the maximum wavenumber recovered without ambiguity is $k_{z_{\max}} = \pi/\Delta_z$, Δ_z being the minimum axial separation distance between microphones. Another limitation concerns the resolution in the wavenumber domain, which is a lower limit related to the spatial extent of the array by $\Delta_{k_z} = 2\pi/L_z$, with L_z the array length. The discretised version of Eq. (6) then writes:

$$\hat{p}(z) = \sum_{k_z=-k_{z_{\max}}}^{k_{z_{\max}}} D_{k_z}(r_0, \phi_0) \mathrm{e}^{\mathrm{j}k_z z}. \tag{7}$$

Setting the values of wavenumber components k_z from negative to positive values allows for the separation of waves propagating along both upstream and downstream directions. In addition, hydrodynamic components associated with turbulent boundary layer (TBL) pressure fluctuations are also separated. These are the main advantages of the axial wavenumber approach.

2.2. *Discussion of the mode detection problem*

In the previous subsection three different formulations for decomposing an in-duct pressure field have been discussed. From an experimental point of view, each decomposition must be associated to a given spatial sampling configuration of the pressure field. The complete decomposition into azimuthal and radial modes, see Eq. (1), requires the sampling of at least two independent coordinates, for instance, (ϕ, z) or (ϕ, r). The azimuthal-only decomposition given by Eq. (5) is based upon the sampling over the azimuthal coordinate ϕ. Finally, the decomposition onto wavenumber components, see Eq. (6) requires the sampling over the axial coordinate z. For practical implementation reasons the infinite sums in both Eqs. (1) and (5) must be truncated. For the same reason, the infinite integral in Eq.

(6) must be discretised to be solved in practice, see Eq. (7). For any of the above formulations the associated linear system of equations might be expressed in a matrix-vector notation, written as

$$\mathbf{p} = \mathbf{\Phi c} + \mathbf{n}, \tag{8}$$

with $\mathbf{p} \in \mathbb{C}^K$ a vector of complex pressure coefficients (as returned from a Fourier transform) at a given frequency ω, $\mathbf{n} \in \mathbb{C}^K$ accounts for additive noise, $\mathbf{c} \in \mathbb{C}^L$ a vector containing the *unknown* complex coefficients and $\mathbf{\Phi} \in \mathbb{C}^{K \times L}$ a matrix whose entries depend on the problem being solved, see Eqs. (1), (5) or (7). For the complete azimuthal and radial mode decomposition (ARMD), see Eq. (1), the dimension L is equal to $2(2M + 1)(N + 1)$ with M and N being respectively the highest azimuthal and radial orders of cut-on modes. The (multiplicative) factor 2 accounts for the downstream $A^+_{m,n}$ and the upstream $A^-_{m,n}$ modes. For the azimuthal-only decomposition (AMD), see Eq. (5), the unknown coefficients are C_m and the dimension L is equal to $(2M + 1)$, with M the highest resolved azimuthal order given by a microphone array configuration. For the wavenumber decomposition (WND), see Eq. (7), the unknown coefficients are D_{k_z} and the dimension L depends on the discretisation parameters $k_{z_{\max}}$ and Δ_{k_z} that are given by the spatial sampling of the pressure field. A summary of the three different formulations is given in Table 1 for the sake of clarity. Note that for AMD and WND the associated matrix $\mathbf{\Phi}$ is independent of the frequency ω, contrary to the ARMD approach. The values for both M and $k_{z_{\max}}$ are set for the highest frequency, given by the microphone array configuration, and are used for the whole frequency band. Furthermore, whereas the axial wavenumber k_z for the WND is based on a continuous distribution (discretised here for solving the problem numerically) the axial wavenumber $k_{z_{m,n}}$ takes only discrete values for each particular mode of azimuthal and radial orders m and n respectively, as given in Eq. (2). Thus, as discussed in Section 2.1, it can be seen that in order to minimise model mismatches, a good estimate of the sound speed c and the mean flow velocity U_0 are required for the ARMD approach. In turn, both AMD and WND approaches do not depend on any estimate of physical quantities, the price to pay is the limited amount of information (i.e. lack of radial order and no separation between downstream and upstream modes for AMD).

Method	Generic elements of $\mathbf{\Phi}$	Unknowns	Comments	Requirement
AMD	$\left\{ \mathrm{e}^{\mathrm{j}m\phi} \right\}$	C_m	$m \in \mathbb{Z}$, $\{-M, M\}\ \forall\omega$	Sampling of ϕ
WND	$\left\{ \mathrm{e}^{\mathrm{j}k_z z} \right\}$	D_{k_z}	$k_z \in \mathbb{R}$, $\left\{-k_{z_{\max}} : \delta_{k_z} : k_{z_{\max}}\right\}\ \forall\omega$	Sampling of z
ARMD	$\left\{ \begin{array}{c} \mathrm{e}^{\mathrm{j}k^+_{z_{m,n}} z} f_{m,n}(r)\mathrm{e}^{\mathrm{j}m\phi} \\ \mathrm{e}^{\mathrm{j}k^-_{z_{m,n}} z} f_{m,n}(r)\mathrm{e}^{\mathrm{j}m\phi} \end{array} \right\}$	$\left\{ \begin{array}{c} A^+_{m,n} \\ A^-_{m,n} \end{array} \right\}$	m and n for cut-on modes only, varying with frequency ω	Sampling of (ϕ,z) or (ϕ,r)

Table 1: Summary of the different formulations allowing the decomposition of cylindrical duct wall-pressure fluctuations.

Finally the goal is to solve Eq. (8) for the *unknown* coefficients $\mathbf{c}$. Whenever the assumption of stationarity and ergodicity of time signals holds, the expression in Eq. (8) can be conveniently written in terms of the cross-spectral matrix of measurements, written by definition as $\mathbf{S_{pp}} \triangleq \mathbb{E}\{\mathbf{pp}^H\}$. The notation $\cdot^H$ denotes the conjugate transpose or the Hermitian of a vector and $\mathbb{E}\{\cdot\}$ stands for the expected value. Equation (8) then reads

$$\mathbf{S_{pp}} = \mathbf{\Phi S_{cc} \Phi}^H + \mathbf{S_{nn}}, \tag{9}$$

with $\mathbf{S_{cc}} \triangleq \mathbb{E}\{\mathbf{cc}^H\}$ the cross-spectral matrix of mode or wavenumber coefficients and $\mathbf{S_{nn}} \triangleq \mathbb{E}\{\mathbf{nn}^H\}$ the cross-spectral matrix of measurement noise. The quantities of interest are often the squared moduli of the mode amplitudes, which are simply given by the diagonal terms of $\mathbf{S_{cc}}$. Off-diagonal terms are the cross-spectra between modal coefficients and are of interest when mutual coherence between modes is expected, for instance at tonal frequencies. Several techniques and algorithms [47, 48] exist to solve the problem in Eq. 9, some of which, such as beamforming solve for each mode independently, whereas others, such as inverse methods, solve the problem as a whole.

For classical beamforming, which assumes incoherent sources, a typical implementation is the Least-Squares Beamforming [49]. The solution coefficients can be written as

$$\hat{c}_l = \frac{\boldsymbol{\phi}_l^H \mathbf{S_{pp}} \boldsymbol{\phi}_l}{\left\| \boldsymbol{\phi}_l \right\|_2^4}, \tag{10}$$

where $\boldsymbol{\phi}_l$ is the l-th column of matrix $\mathbf{\Phi}$ and the notation $\|\mathbf{x}\|_2^4$ stands for the ℓ_2-norm or the Euclidean norm of the vector $\mathbf{x}$ at the 4-th power. The $\hat{c}_l$ is the auto-spectrum associated to the l-th mode or wavenumber coefficient.

Notice that this approach does not give an estimate of the full cross-spectral matrix of modal coefficients $\hat{\mathbf{S}}_{\mathbf{cc}}$ due to the aforementioned assumption. The advantages of beamforming are its robustness and computational speed. However, a limited resolution and poor quantification results are well-known limitations of beamforming. Inverse methods and deconvolution approaches are alternatives to overcome beamforming limitations at the expense of a higher computational cost. An iterative Bayesian Inverse Approach (iBIA) is applied in the present work. This method has recently been applied to the localisation and quantification of aeroacoustic sources, such as jet noise [47] and airframe noise [50, 48]. Theoretical aspects of iBIA are recalled in the next section.

2.3. Overview of the Bayesian formalism

The central idea of the Bayesian framework is to consider all variables within a problem as stochastic (random) processes. Thus, both the unknowns $\mathbf{c}$ and observations $\mathbf{p}$ are considered as random variables which are modelled through probability density functions (PDF). Bayes' theorem allows to express the solution of the inverse problem, or the posterior PDF $[\mathbf{c}|\mathbf{p}]$ of the vector $\mathbf{c}$ given the measurements $\mathbf{p}$ as:

$$[\mathbf{c}|\mathbf{p}] = \frac{[\mathbf{p}|\mathbf{c}][\mathbf{c}]}{[\mathbf{p}]}, \tag{11}$$

where $[\mathbf{p}|\mathbf{c}]$ reflects the probability of observing the data for a given instance of $\mathbf{c}$ (the likelihood model), $[\mathbf{c}]$ is the prior distribution and $[\mathbf{p}]$ is the marginal distribution of the observations, the so-called "evidence". The approach then reduces to modelling the PDFs $[\mathbf{p}|\mathbf{c}]$ and $[\mathbf{c}]$ based on the specifics of the problem and using (11) to solve for the posterior PDF $[\mathbf{c}|\mathbf{p}]$. In acoustics, Bayesian approaches have been initially applied to noise source reconstruction [51] and localisation methods [52]. More recently, they have been applied to the modal identification problem by Roncen *et al.* [53], where the inference of both the modal amplitudes and the flow profile has been successfully determined using synthetic noise signals. The approach has been constrained to the over-determined case, that is, the number of microphones being greater than the number of unknown modes and a Markov chain Monte Carlo (MCMC) algorithm used to solve the inference problem.

Before applying this approach to modal detection a few consequences of duct mode properties onto the mathematical modelling are underlined hereafter. Unlike source localisation problems that are ill-conditioned due to their back-propagation step, especially at low frequencies [54, 55], duct mode identification exhibits a different behaviour due to the cut-off/cut-on effect imposed by the duct geometry and influenced by the mean flow. Indeed, only a finite number of modes propagate at a given frequency and this number increases with frequency according to the dispersion relation. At the mode cut-off frequency, that is, the frequency at which the mode switches from cut-off to cut-on, the axial wavenumber becomes small and the axial wavelength very large. Thus even for axially long arrays, the microphones sense almost the same information, and the condition number becomes very high. As frequency increases, more and more modes become cut-on and the condition number tends to increase. Thus, one expects small condition numbers at lower frequencies and large ones at higher frequencies [35], that will require regularisation of the problem.

2.4. Bayesian model of the mode detection problem

Similarly to Refs. [56, 57] the measurement noise $\mathbf{n}$ in Eq. (8) is modelled here as a complex Gaussian distribution, with the notation $\mathcal{N}_{\mathbb{C}}(\mathbf{n}; \mathbf{0}, \gamma^2\mathbf{I}_K)$ to be read as the vector $\mathbf{n}$ following a complex Gaussian with zero mean vector $\mathbf{0}$ and covariance matrix $\mathbb{E}\{\mathbf{n}\mathbf{n}^H\} = \gamma^2\mathbf{I}_K$, where $\mathbf{I}_K$ is the identity matrix of dimension K and γ^2 is the power of the noise signal. Thus, it is assumed *a priori* that the noise field is homogeneous. It then results that the likelihood PDF also follows a complex Gaussian

$$[\mathbf{p}|\mathbf{c}] = \mathcal{N}_{\mathbb{C}}(\mathbf{p}; \mathbf{\Phi c}, \gamma^2\mathbf{I}_K) \propto \mathrm{e}^{-\gamma^{-2}\|\mathbf{p}-\mathbf{\Phi c}\|_2^2}, \tag{12}$$

where the sign "proportional to" has been used in the last term since the normalisation constant has been omitted for the sake of simplicity. It should be underlined that only terms that impact the posterior maximization are kept. The modelling of the prior distribution involves much more flexibility and should translate any *a priori* information about the solution known to the user. If this is not the case, non-informative priors such as the uniform distribution are to be used, such as the approach followed by Roncen *et al.* [53]. It has been shown that the choice of a complex Gaussian distribution leads to a maximum a posteriori (MAP) estimate equivalent to the classic Tikhonov regularisation [51, 56]. Modelling the prior PDF as a Generalised Multivariate Complex Gaussian (GMCG) gives

$$[\mathbf{c}] \propto \mathrm{e}^{-\alpha^{-p}\sum_{i=1}^{L}|c_i|^p} = \mathrm{e}^{-\alpha^{-p}\|\mathbf{c}\|_p^p}, \tag{13}$$

where $0 < p \leq 2$ is the (integer) shape parameter, α is the scaling parameter and it is assumed that $\mathbf{c}$ has a zero mean. The notation of the sum in the exponential is simplified by defining the ℓ_p norm of the vector $\mathbf{c}$ as $\|\mathbf{c}\|_p = (\sum_{i=1}^{L} |c_i|^p)^{1/p}$. Given the probability models of both the likelihood and the prior, the next step is then to apply Bayes rule, see Eq. (11), to infer the posterior PDF and particularly the value of highest probability, which is commonly referred to as the MAP estimate. Plugging Eqs. (12) and (13) into Eq. (11) leads to

$$\begin{aligned}\hat{\mathbf{c}} &= \arg\max_{\mathbf{c}} \{[\mathbf{p}|\mathbf{c}][\mathbf{c}]\} \\ &= \arg\min_{\mathbf{c}} \{-\ln([\mathbf{p}|\mathbf{c}][\mathbf{c}])\} \\ &= \arg\min_{\mathbf{c}} \left\{\gamma^{-2}\|\mathbf{p} - \mathbf{\Phi c}\|_2^2 + \alpha^{-p}\|\mathbf{c}\|_p^p\right\}, \end{aligned} \tag{14}$$

where in the second equality, maximisation was converted into minimisation by taking the opposite of the logarithm. Notice that the "evidence" $[\mathbf{p}]$ has been omitted in the first equality since it does not depend on $\mathbf{c}$. By defining $\eta^2 = \gamma^2/\alpha^{-p}$ as the regularisation parameter, the MAP estimate leads to the following minimization problem

$$\hat{\mathbf{c}} = \arg\min_{\mathbf{c}} \left\{\|\mathbf{p} - \mathbf{\Phi c}\|_2^2 + \eta^2\|\mathbf{c}\|_p^p\right\}, \tag{15}$$

that associates the ℓ_2 and the ℓ_p norms in the penalty term. Except for the case $p = 2$, there is no closed form solution of this minimisation problem. The choice of $p < 2$ leads to PDFs having more mass both at zero and in the tails. This will indeed favour sparse solutions $\hat{\mathbf{c}}$, that is, with a few large-amplitude coefficients and a great number of small-amplitude coefficients. It is noteworthy to mention that a somewhat different approach has been recently followed by Antoni et al. [57] that resulted in the iterated Bayesian focusing algorithm. Indeed a hierarchical Bayesian model has been employed by modelling the so-called aperture function as a random variable. The aperture function is well suited for noise source reconstruction or localization problems since sound typically emanates from specific source regions within a large search domain. The approximate location of these regions is often known a priori. Various probability distribution laws promoting sparsity have been evaluated [57]. In particular it has been shown that priors leading to ℓ_1-norm penalties promote solutions showing a weaker sparsity as compared to other priors such as the multivariate complex Student-t or the generalised multivariate complex Gaussian with ℓ_0-norm penalty.

Considering the problem examined herein, it is well-known that tonal and broadband fan noise have distinct modal content. Tonal noise is known to be generated by constructive interference phenomena that excite specific mode patterns depending on the noise generation mechanism. Thus, it is expected *a priori* that choices of $p \to 0$ will lead to improved results for tonal mode detection. A different behaviour is observed for broadband noise, as its energy tends to spread over a large number of mode coefficients. Nevertheless, the actual sparsity is found to be different due to the experimental practices and the "filter" effect of the duct. It is common practice to place the microphone arrays several wavelengths away from the actual sources and duct discontinuities. As discussed in Section 2.1 only a finite number of modes propagate away from the sources due to the duct dispersion relation. Most of the modes, the cut-off modes, decrease exponentially and are not captured by the microphone array. On the other hand, with the use of more and more dense microphone arrays the actual range of covered modes is commonly about a hundred of mode orders. It results that over a wide frequency range the number of actual cut-on modes is much smaller than the number of modes in the modal extent, that is, the domain in which modes are "searched". In addition, previous studies show that the propagation of fan broadband noise through fan blades and OGV rows introduces distinctive features in the mode-frequency spectra, for instance the predominance of co-rotating or counter-rotating modes leading to modal distributions that deviate from a uniform distribution of energy. The approach followed in this work is thus to set the GMCG prior with an assumption of mild sparsity by solving Eq. (15) with $p = 1$. Given the above remarks, the interest is now on how to devise an algorithm to solve Eq. (15). This is the subject of the next subsection.

2.5. The implemented algorithm

It has been discussed in the previous section that no closed-form solution exists for the minimisation problem in Eq. (15). Nevertheless, an algorithm to solve it can be devised by employing the majorisation-minimisation (MM) principle [58]. The goal is to find a quadratic function that majorises the initial cost function and then to minimise it.

The price to pay for the simplification is an iteration process. It can be shown that a majorising function for Eq. (15) is

$$J(\mathbf{c}) = \arg\min_{\mathbf{c}} \left\{ \|\mathbf{p} - \mathbf{\Phi c}\|_2^2 + \eta^2 \|\mathbf{W}^{-1}\mathbf{c}\|_2^2 \right\}, \tag{16}$$

with $\mathbf{W}$ being a diagonal matrix with generic elements $\lceil w_i \rfloor = \left|\hat{c}_{i,[k-1]}\right|^{1-\frac{p}{2}}$ to be read as the i-th element of the solution $\hat{\mathbf{c}}_{[k-1]}$ at the iteration $k-1$. The solution of the problem consists of iteratively solving Eq. (16) with updated weights $\lceil w_i \rfloor$ at each iteration k. The derived algorithm is closely related to the FOCal Underdetermined System Solver (FOCUSS) [59], based on a weighted minimum norm solution of an underdetermined problem and on the iteratively reweighed least squares (IRLS) algorithm [60]. The advantage of the Bayesian formalism over other approaches is that it provides an intrinsic way of adjusting the regularisation parameter η^2 in Eq. (16). This is not an easy task and several *ad-hoc* techniques for setting η^2 have been proposed in the literature, the Generalized Cross-Validation (GCV) [61] and the L-curve [62] are well-known examples. There is a vast literature on the use of these techniques for inverse problems in acoustics [63, 64, 55]. The approach to determine η^2 within a Bayesian formalism is discussed in ref. [56] and applied in the present work.

The solution of the minimisation problem in Eq. (16) is written

$$\hat{\mathbf{c}} = \lceil \mathbf{W} \rfloor^2 \mathbf{\Phi}^H \left(\mathbf{\Phi} \lceil \mathbf{W} \rfloor^2 \mathbf{\Phi}^H + \eta^2 \mathbf{I} \right)^{-1} \mathbf{p}, \tag{17}$$

where $\mathbf{I}$ is the identity matrix. In practice, advantage is taken of the fact that the measurements may be assumed as being stationary and ergodic to work rather with the cross-spectral matrix $\mathbf{S_{pp}}$. The solution then is written:

$$\hat{\mathbf{S}}_{\mathbf{cc}} = \mathbf{\Psi}^{\ddagger} \mathbf{S_{pp}} (\mathbf{\Psi}^{\ddagger})^H, \tag{18}$$

with the regularized inverse matrix $\mathbf{\Psi}^{\ddagger}$ defined as $\mathbf{\Psi}^{\ddagger} = \lceil \mathbf{W} \rfloor^2 \mathbf{\Phi}^H (\mathbf{\Phi} \lceil \mathbf{W} \rfloor^2 \mathbf{\Phi}^H + \eta^2 \mathbf{I})^{-1}$. The matrix $\mathbf{\Psi}^{\ddagger}$ may also be conveniently expressed in terms of the following singular value decomposition (svd)

$$[\mathbf{\Phi W}] \overset{\text{svd}}{=} \mathbf{U} \lceil \mathbf{S} \rfloor \mathbf{V}^H, \tag{19}$$

where $\mathbf{U} \in \mathbb{C}^{K \times K}$ and $\mathbf{V} \in \mathbb{C}^{L \times K}$ are two unitary matrices stacking left and right singular vectors respectively, and $\lceil \mathbf{S} \rfloor \in \mathbb{R}^{K \times K}$ is a diagonal matrix with singular values sorted in descending order. Thus, the regularized inverse matrix $\mathbf{\Psi}^{\ddagger}$ also writes:

$$\mathbf{\Psi}^{\ddagger} = \lceil \mathbf{W} \rfloor \mathbf{V} \left[s_k + \frac{\eta^2}{s_k} \right]^{-1} \mathbf{U}^H, \tag{20}$$

where s_k is the k-th diagonal element of $\lceil \mathbf{S} \rfloor$. The decomposition from Eq. (19) is also useful for adjusting the regularisation parameter η^2 [56]. The optimal regularisation parameter is obtained from the data by minimising the following cost function

$$\hat{\eta}^2 = \arg\min_{\eta} J_{\text{MAP}}(\eta^2)$$
$$J_{\text{MAP}}(\eta^2) = \sum_{k=1}^{K} \ln\left(s_k^2 + \eta^2\right) + (K-2) \ln\left[\frac{1}{K} \left(\sum_{k=1}^{K} \frac{\langle |y_k|^2 \rangle}{s_k^2 + \eta^2} \right) \right], \tag{21}$$

where the term $\langle |y_k|^2 \rangle$ stems from a projection of the measurements onto the array subspace given by $\langle |y_k|^2 \rangle = \mathbf{u}_k^H \mathbf{S_{pp}} \mathbf{u}_k$, with $\mathbf{u}_k$ being the k-th column of matrix $\mathbf{U}$ given by the decomposition in Eq. (19). The minimisation of this cost function is simply done by a simple grid search method for instance and carried out for each frequency separately.

3. Overview of the experimental test campaign

3.1. Description of the test bench

The experimental campaign has been carried out at the Universal Fan Facility for Acoustics (UFFA) test rig operated by AneCom AeroTest. An extensive database of both acoustic [65, 66] and aerodynamic data [67] has been

acquired. A sketch of the ducted test-section in Figure 2 depicts the position of mode detection rings relative to the fan-OGV system. In the present work, the azimuthal ring CMD1 at the intake as well as the azimuthal ring CMD3 and the axial line array (AX1) in the bypass section downstream of the Outlet Guide Vanes (OGV), are of particular interest.

The tested fan has 20 blades and a diameter of 0.864 m. A set of 44 OGVs is placed at two different axial positions defining two machine configurations. The first position corresponds to a nominal gap between fan and OGVs whereas for the second one the fan-OGV gap is increased. The first configuration is hereafter referred to as the Short-Gap (SG) configuration and the latter as the Long-Gap (LG) configuration. The measurements have been acquired at various rotational speeds for two Working Lines (WL). The first WL is a Sea Level Static Working Line (SLSWL) and the second one a low noise working line (LNWL). The SLS working line is representative of sea level static conditions, whereas the LN is obtained by increasing the mass flow through the bypass section leading to an increase in the axial flow velocity in the inlet. This in turn reduces the incidence on the fan blades which are then less loaded and the rotor pressure-ratio is reduced. Less loaded blades are likely to have thinner and less turbulent wakes and it is thus expected that broadband noise sources are mitigated.

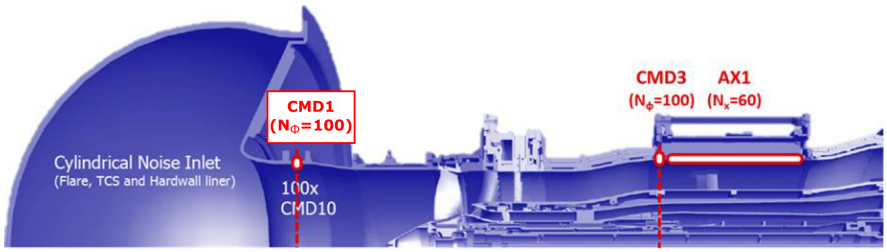

Figure 2: Sketch of the test section at the UFFA test rig operated by AneCom AeroTest. The picture highlights the position of microphone arrays used in this work. They are located both at the intake (CMD1) and in the bypass duct (CMD3 and AX1).

3.2. *Description of the microphone arrays*

The test bench has been equipped with various mode detection rings. The goal was to characterise the modal content at the intake, inter-stage and at the by-pass section downstream of OGVs. The intake is equipped with a ring of 100 kulite® XCS-190 pressure transducers distributed non-uniformly along the duct circumference. The azimuthal distribution of probes has been optimised using the procedure presented by Rademaker *et al.* [18]. This configuration allows for the capture of the azimuthal modal content up to an azimuthal order of $m = \pm 79$ with reduced aliasing. The bypass duct is equipped with a mode detection ring (CMD3) combined with an axial linear array (AX1). The azimuthal ring is equipped with 100 Endevco® 8510C piezoresistive pressure transducers. As for the CMD1 array, the probes are non-uniformly distributed along the outer duct casing, allowing for a decomposition up to azimuthal order $m = \pm 79$. The axial linear array is composed of 60 regularly spaced G.R.A.S® 40BP pressure microphones. The array axial extent is $L_z = 796$ mm, and the inter-microphone spacing is $\Delta_z = 13.5$ mm.

During the experimental campaign a few probes experienced failure during the tests depending on the measured operation conditions. This has been observed for the arrays both at the intake and the bypass ducts. The intake ring array has shown up to 12 sensor failures and the bypass duct ring array up to 7. Thus, the performance of the degraded arrays has been checked accordingly. This has been done by evaluating a parameter called mutual coherence of the modal matrix $\mathbf{\Phi}$. In short, it characterises the dependence between columns of the matrix $\mathbf{\Phi}$. It is given by the largest normalised inner product between different columns

$$\mu(\mathbf{\Phi}) = \max_{i \neq j} \frac{\left| \boldsymbol{\phi}_i^H \boldsymbol{\phi}_j \right|}{\|\boldsymbol{\phi}_i\|_2 \|\boldsymbol{\phi}_j\|_2}, \tag{22}$$

with $\boldsymbol{\phi}_i$ the i-th column of matrix $\mathbf{\Phi}$ and the notation $\|\mathbf{x}\|_2$ being the ℓ_2-norm or the Euclidean norm of the vector $\mathbf{x}$. The comparison between the baseline and reduced arrays for both the intake and bypass mode detection rings is given in Fig. 3. For the sake of comparison, the mutual coherence from a regularly-spaced ring of 100 microphones

is also shown. It can be seen that when the Shannon-Nyquist is no longer satisfied the mutual coherence exhibits a sudden jump from 0 to 1 and a strong "coherent" aliasing occurs. The use of irregularly spaced arrays is shown to increase the limit of resolved azimuthal orders (here from 50 to 79) at the expense of a slight increase of the mutual coherence at low orders as compared to the regular case. This increase indeed produces a sort of "incoherent" aliasing with replicated components distributed over the whole azimuthal and frequency domains (see Figs. 5(a) and 5(b) for instance). The use of sparsity-based reconstruction algorithms is able to efficiently remove these replicas, see Fig. 5(c) for instance. The results in Fig. 3 show that although the azimuthal order upper-limit of m = 79 is not altered by the failing probes, the mutual coherence increases for lower azimuthal orders. This means that the aliasing artefacts due to sidelobes are also increased. Indeed, as shown elsewhere [68] the mutual coherence is equivalent to the maximum of the sidelobe-to-peak ratio as commonly used in the array signal processing community. The modal analyses shown in the next sections have been obtained after carefully removing the failing sensors. The axial line array did not experience any sensor failure during the test campaign.

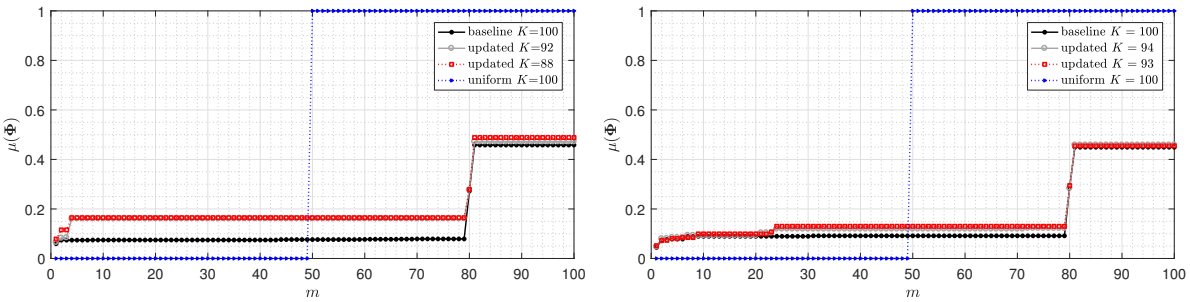

(a) intake ring array

(b) bypass ring array

Figure 3: Mutual coherence of the baseline and degraded mode detection rings considering sensor failure. Results are shown for (a) CMD1 intake array (b) CMD3 bypass array. For the sake of comparison the mutual coherence of a regularly spaced array of 100 probes is also represented.

4. Results and discussion

4.1. Single-out fan broadband noise through cyclostationary tools

In order to focus the analysis on fan broadband noise a technique to separate tonal and broadband noise is applied to the measured data [69]. A tachometer trigger delivering one-pulse per revolution signal is used to resample the wall-pressure time signals. This step ensures a regular number of time samples per rotor revolution. The resampled data is then averaged over one or more rotor cycles, depending on the required angular frequency resolution. The deterministic signal obtained in the previous step is then subtracted from raw angular signals. The result is a residual signal from which the 1st order cyclostationary part has been removed. This residual signal contains 2nd and higher order cyclostationary components. Examples of spectra obtained following this procedure are shown in Fig. 4. All the modal analyses presented hereafter have been obtained from data following this procedure of tone removal.

4.2. Comparison of mode detection techniques

A comparison between different mode detection techniques is given in this section. Three approaches are compared here, namely Least-Squares Beamforming given by Eq. (10), a classic inverse method with ℓ_2-norm penalty that indeed is comparable to iBIA approach with $p = 2$ and finally iBIA approach with $p = 1$. Figure 5 summarises the results obtained at the 100%ND (where ND stands for Nominal Drive and ND = 7597 rpm) fan speed for the noise measured at the intake duct. The results are presented as 2D color plots of azimuthal mode amplitudes as a function of mode order and frequency. Figure 5 shows that for both the Beamforming and classic inverse methods, the mode amplitude estimates are biased by aliased data. In addition, given the axial positioning of the CMD1 microphone array, which is far away from the source, levels outside the cut-on triangle are expected to be very low. The overlapping of sidelobes or aliased data into the cut-on triangle hinders a correct estimate of mode amplitudes. Conversely, results obtained by iBIA with $p = 1$ show a good "cleaning" of aliased data and thus a correct estimate of mode amplitudes

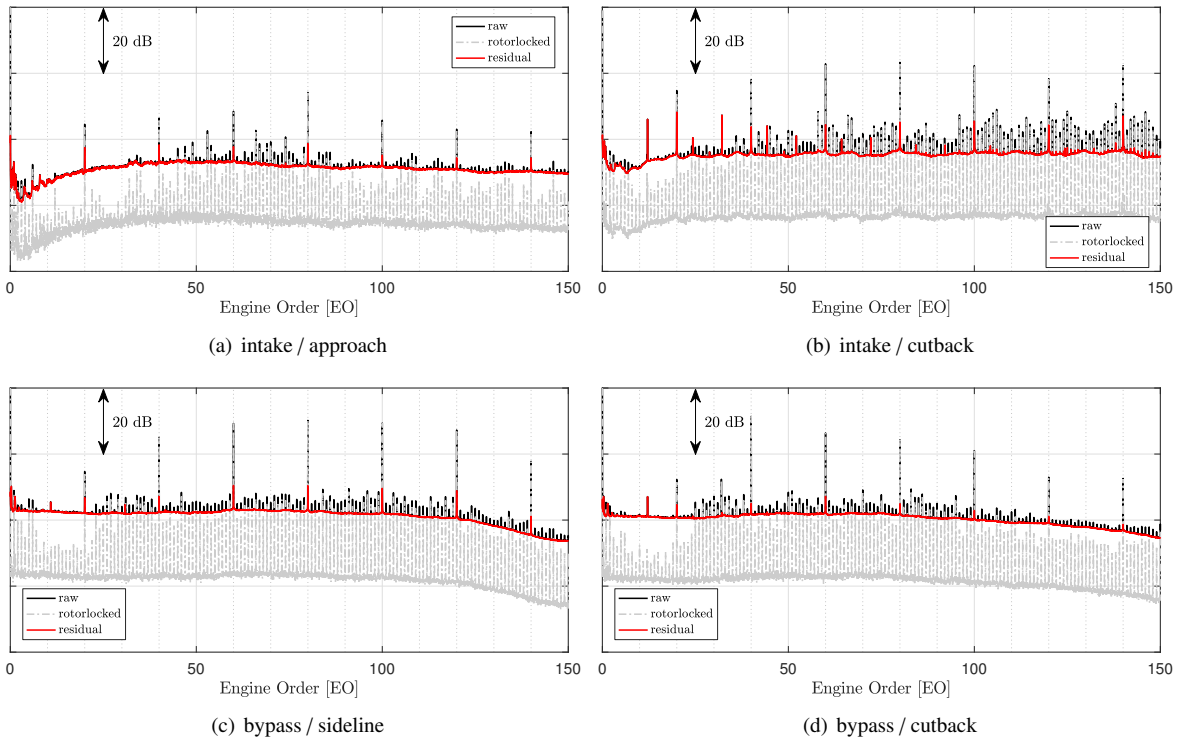

(a) intake / approach (b) intake / cutback

(c) bypass / sideline (d) bypass / cutback

Figure 4: Results of the procedure to extract 1st order cyclostationnary component (rotor-locked field) from wall-pressure fluctuations. The residual component in red colour is of particular interest in this work. The results are shown for different positions in the duct and different operating points, namely: (a) at the intake and approach condition 50%ND, where ND stands for "Nominal Drive"; (b) intake and cutback condition 80%ND; (c) at the bypass duct and sideline condition 90%ND and (d) at the bypass duct and cutback condition 80%ND. The results are given for the short fan-OGV gap and at the sea level static working line (SG-SLSWL).

and a better dynamic range. Note that the same range of pressure levels is used for the three methods. The comparison is also done for a lower rotational speed corresponding to 70%ND. The results are summarised in the Fig. 6. It can be seen that cutoff levels are well attenuated by the iBIA approach showing a good improvement of the dynamic range. The analyses in the next sections are carried out with the $p = 1$ based iBIA approach.

4.3. Intake azimuthal mode analysis

The azimuthal modal content at the intake is computed by solving Eq. (5) using the iBIA algorithm with data from the microphone ring CMD1 (see Figure 2). The results are shown for the short-gap fan-OGV configuration both at the sea level static working line (SG-SLSWL) and the low noise working line (SG-LNWL), see Figures 7 and 8 respectively. The azimuthal modal content is shown for three values of the engine power corresponding to certification points, namely: approach (50% ND), cutback (80% ND) and sideline (90% ND). The blade tip rotation Mach number computed at the rotor leading edge is equal to $M_t = 0.5$ at approach, $M_t = 0.81$ at cutback and $M_t = 0.91$ at sideline. Note that tonal components have been extracted following the procedure of Sec. 4.1.

As expected the sound pressure levels are concentrated within the mode-frequency cut-on triangle, since cut-off modes are well attenuated given the distance between the inlet array and the rotor blades. It is observed that the broadband component increases with fan speed up to the 70% ND operating point (see Fig. 6(c)) and then starts to decrease. A different trend is observed for the downstream noise measured at the bypass duct as shown by the results to be presented in the next section (see Fig. 12). The helical tip Mach number [70] $M_{\mathrm{Hel}} = \sqrt{M_t^2 + M_z^2}$ evaluated at both the cutback and sideline conditions is $M_{\mathrm{Hel}} = 0.93$ and $M_{\mathrm{Hel}} = 1.04$ respectively, suggesting a possible generation of shock waves at the rotor blades. This has been confirmed by a Reynolds-averaged Navier-Stokes (RANS) simulation of the current configuration recently reported by Blázquez-Navarro and Corral [71]. Rotor shock waves are known to

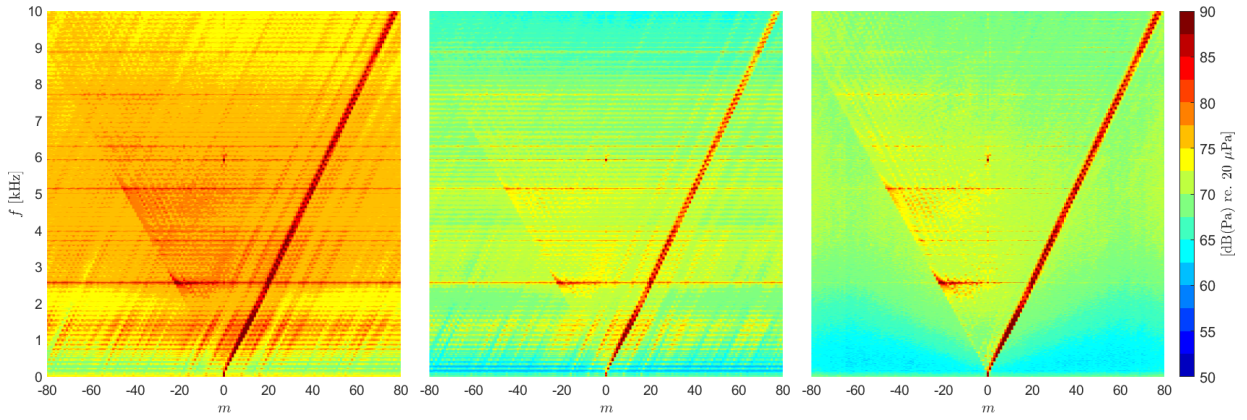

(a) beamforming (b) classic ℓ_2-norm (c) iBIA ℓ_p-norm with $p = 1$

Figure 5: Example of azimuthal mode detection plots at the intake for three different methods at 100%ND fan speed. Results are given for three methods, namely: (a) Least-Squares Beamforming, (b) classic ℓ_2 regularisation and (c) iBIA with $p = 1$. Results are for the short gap rotor/stator configuration at the sea level static working line (SG-SLSWL). The frequency is plotted against the azimuthal mode order and the modes are coloured by their amplitude.

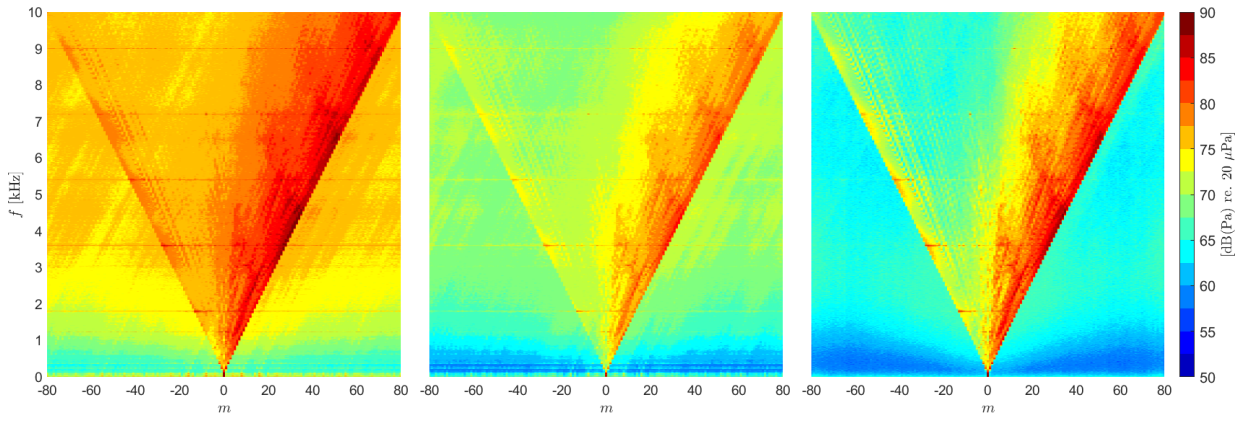

(a) beamforming (b) classic ℓ_2-norm (c) iBIA ℓ_p-norm with $p = 1$

Figure 6: Example of azimuthal mode detection plots at the intake for three different methods at 70%ND fan speed. Results are given for three methods, namely: (a) Least-Squares Beamforming, (b) classic ℓ_2 regularisation and (c) iBIA with $p = 1$. Results are for the short gap rotor/stator configuration at the sea level static working line (SG-SLSWL). The frequency is plotted against the azimuthal mode order and the modes are coloured by their amplitude.

block the passage of downstream generated noise travelling upstream across the rotor disk. In addition, the acoustic shielding effect by the fan rotor on the downstream noise is seen to increase with the rotor speed as shown by the same authors [71]. Another distinct feature is that co-rotating modes ($m > 0$ rotating in the same direction as the fan) prevail in the mode-frequency spectrum. By reasoning in terms of equivalent dipoles, this co-rotating mode distribution is likely to originate from the impact of turbulence from rotor wakes into the OGV's leading edge. A sketch showing a rotor blade and a few OGVs along with the orientation of edge dipoles is shown in Fig. 9. From this simplified representation, it is expected that noise sources at the stator leading edge will tend to favour co-rotating modes when considering upstream propagating noise since the direction of mode propagation is rather aligned with the dipole main lobe. This might explain the bias towards co-rotating modes seen at the inlet mode plots mainly at approach and cutback conditions.

It can also be noticed that an aliasing of co-rotating mode amplitudes onto negative azimuthal orders m happens at higher frequencies, in particular above 10 kHz (see top left corner in the mode frequency plots). This is related to the

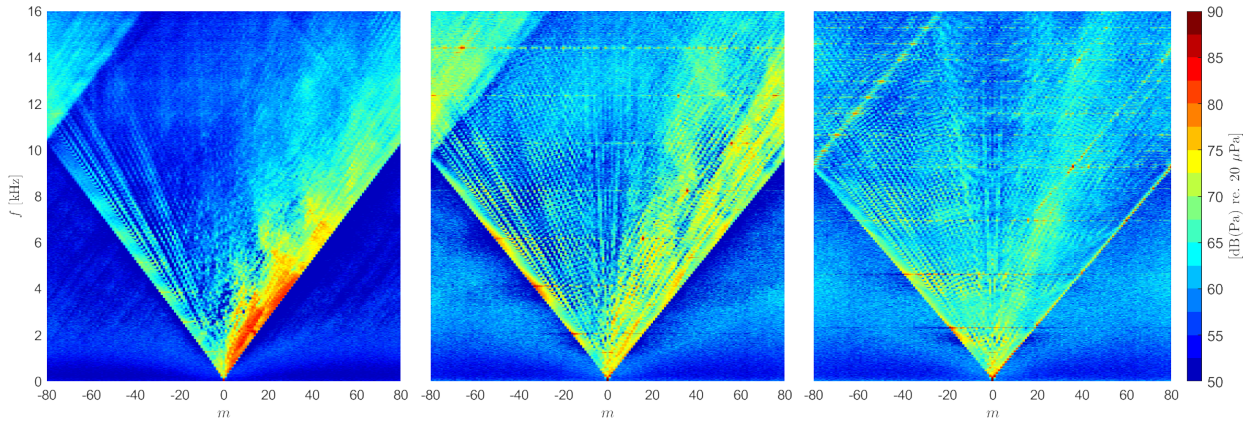

(a) approach (b) cutback (c) sideline

Figure 7: Azimuthal mode detection plots at the intake for three certification points. Results are given for three operating points, namely: (a) approach 50%ND, (b) cutback 80%ND and (c) sideline 90%ND. Results are for the short gap rotor/stator configuration at the sea level static working line (SG-SLSWL). The frequency is plotted against the azimuthal mode order and the modes are coloured by their amplitude.

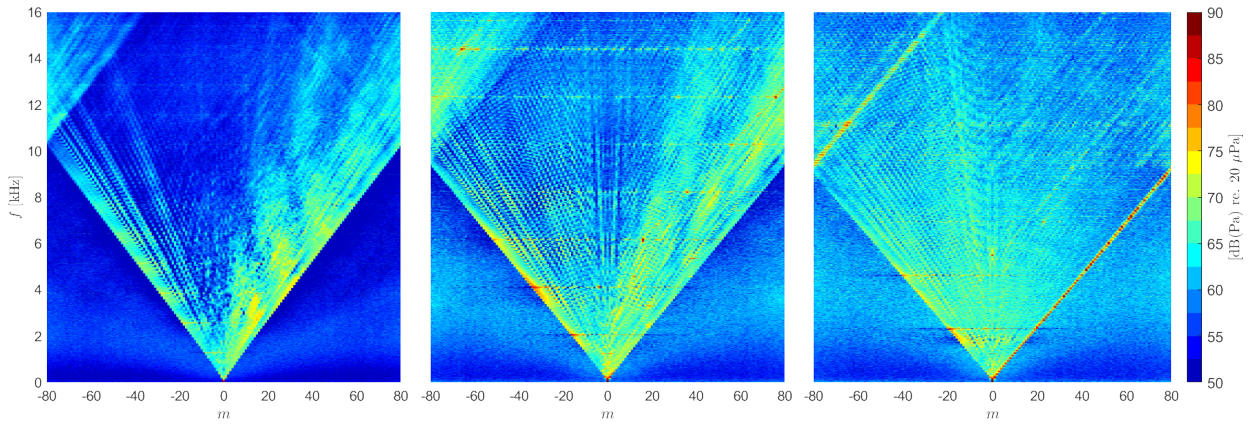

(a) approach (b) cutback (c) sideline

Figure 8: Azimuthal mode detection plots at the intake for three certification points. Results are given for three operating points, namely: (a) approach 50%ND, (b) cutback 80%ND and (c) sideline 90%ND. Results are for the short gap rotor/stator configuration along the low noise working line (SG-LNWL). The frequency is plotted against the azimuthal mode order and the modes are coloured by their amplitude.

azimuthal order limit given by the array geometry which is $m = 79$, see Fig. 3(a). The aliasing starts for frequencies above which modes with azimuthal order $m > 79$ become cut-on and cannot be resolved by the array. Thus, care must be taken when evaluating mode amplitude plots at those frequencies.

A remarkably different behaviour is observed by the spinning mode distribution at the 100%ND fan speed, at transonic rotor tip-speeds ($M_t = 1.02$, $M_{Hel} = 1.15$), see Fig. 5(c). Higher levels are seen to be concentrated along a strong oblique line that appears to be close to the cut-on/cut-off boundary of co-rotating modes. Further understanding of this behaviour is given by the analysis shown in Fig. 10. The theoretical mode cut-off frequencies are computed at the CMD1 axial section and superimposed in the mode frequency plot by black dots, see Figure 10(a). It can be seen that the slope of the strong oblique region is steeper than the theoretical cut-on/cut-off boundary. The oblique line follows closely the line defined by the function $m(\omega) = \omega/\omega_R$, ω_R being the rotor-shaft rotational speed, that corresponds to "rotor-alone" modes propagating at supersonic tip speeds. It should be reminded that this modal distribution is computed from the residual part of pressure fluctuations and thus the rotor-locked contribution is filtered out, this can be seen in Fig 10(c). The presence of spectral humps at both sides of the rotor frequency

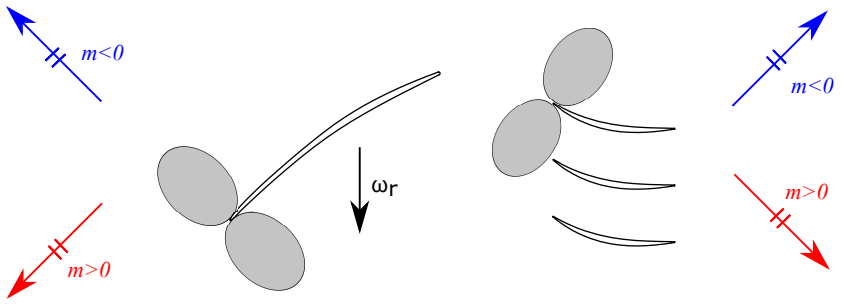

Figure 9: Sketch illustrating the equivalent dipole-like reasoning. The picture shows a rotor blade and three stator vanes, the direction of rotation represented by the ω_r arrow. An illustrative dipole directivity is placed both at the rotor leading edge and the stator leading edge (not taking into account the actual influence of the airfoils onto the directivity in the chordwise direction due to possible non-compactness). The direction of co- and counter-rotating modes propagating either upstream or downstream are depicted by the coloured arrows.

harmonics indicates a modulation of the shaft frequency. A detailed view of the mode frequency plot shown in Fig. 10(b) shows that the energy of the "rotor-alone" mode leaks into the neighbouring spectral humps. The origin of the modulation is still uncertain, however one hypothesis might be the interaction with longitudinal acoustical resonances at very low frequencies that might appear in this kind of installation, see for instance Ref. [72].

In order to quantify the bias towards co-rotating modes for intake mode spectra, the modal amplitudes are summed over co-rotating and counter-rotating modes separately. The resulting spectra are shown in Fig. 11 for approach and cutback power. At lower fan-speeds, the gap between co- and counter-rotating modes is significant, see Fig. 11(a). Several spectral humps, which are not exactly centred at BPF tones, can be distinguished on these spectra. These humps are also present at higher fan speeds, for instance at 60%ND (see Fig. 17(b)) and at cutback power (see Fig. 11(b)), with clear spectral broadening as the speed increases. A similar behaviour has been observed for the inlet duct wall-pressure spectrum by Ganz et al. [73]. It is argued therein that this spectral content might be related to rotor interaction with inlet boundary layer. It could possibly be related to azimuthal inhomogeneities of the casing and hub boundary layers interacting with the rotor blades and generating broadened peaks around the BPFs. Another point is that rotor/casing boundary layer interaction would result in a dipole-like source at the rotor blade leading edges as sketched on Fig. 9. On this figure, it can be seen that sound propagating upstream from such sources will favour counter-rotating modes radiating in the direction of the dipole suction side lobe. Since the humps are much more pronounced for the counter-rotating modes, this explanation strengthens the idea that these humps might be related to the blade/TBL interaction.

It can also be seen that tones remain in the mode spectra from Fig. 11 even after applying the procedure to extract the 1st order cyclostationary component. The results of the extraction procedure are shown in Fig. 4. Particularly at the cutback fan speed, see Fig. 4(b), an extraneous tone appears at a non-integer value of the engine order (EO = 12.15) , that corresponds to a frequency f_e = 1250 Hz. It has been checked during a deceleration manoeuvre that this frequency remains constant when varying the rotor speed ω_R, see also Fig. 13(b), at which the same tone is present at sideline conditions. Moreover, it interacts with the BPFs and generates additional peaks in the spectrum at frequencies $sf_e + k$BPF, with s and k positive integers. Thus it is a non linear coupling that could be due to a (mechanical, acoustic or flow) resonance. Since this deterministic phenomenon is not linearly coupled to ω_R the procedure fails to remove it. The interaction of the resonance with the BPFs is seen to hamper the tone filtering process, contrary to the other tones multiples of the rotor shaft speed, specially at the intake duct. A deeper analysis of the origin of this resonance is required for further conclusions.

4.4. Bypass-duct azimuthal mode analysis

The azimuthal mode-frequency content in the bypass duct downstream of the OGVs is shown in Fig. 12 for the three certification points. The results are obtained using the data from the downstream mode detection ring CMD3 (see Fig. 2). It can be observed that unlike for the intake mode plots no clear trend towards co- or counter-rotating modes exists, except for a shift towards counter-rotating modes well above cut-on, that is, away from the cut-on boundary. As frequency increases higher amplitudes tend to be rather concentrated on modes well above cut-on, with

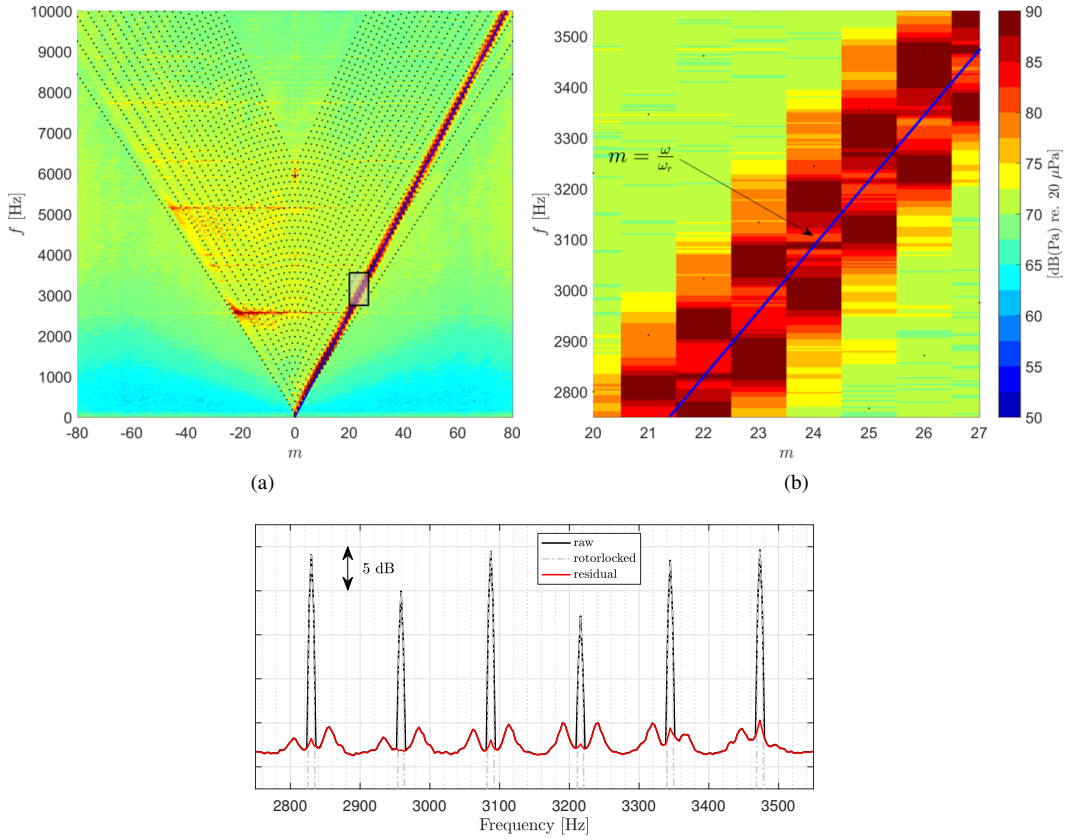

Figure 10: Analysis of the intake azimuthal mode content at the 100% ND rotational speed. Results are given for the short gap rotor/stator configuration at the sea level static working line (SG-SLSWL). (a) The frequency is plotted against the azimuthal mode order and the modes are coloured by their amplitude. The superimposed black dots correspond to the theoretical mode cut-off frequencies computed for the CMD1 duct cross-section. The blue dots show the function $m(\omega) = \omega/\omega_R$. The grey box is a region that is zoomed in and shown in (b), at which the oblique blue line corresponds to $m(\omega) = \omega/\omega_R$. (c) Detailed view of the CMD1 averaged spectrum showing the procedure to extract the rotor-locked contribution from the raw spectrum. The analysis shown in (a) and (b) is computed based on the residual contribution.

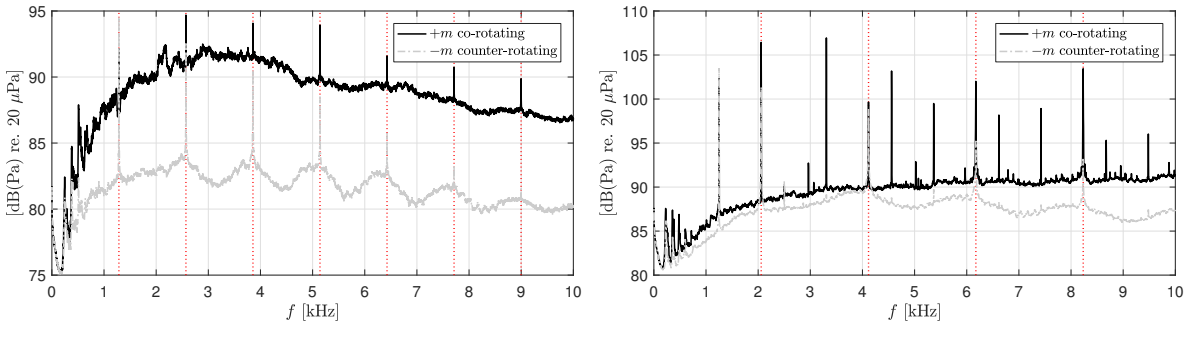

Figure 11: Integrated intake mode spectra over co-rotating ($+m$) and counter-rotating ($-m$) modes for two fan speeds: (a) approach 50%ND and (b) cutback 80%ND. The results are given for the short fan-OGV gap along the sea level static working line (SG-SLSWL). Additional vertical red dotted lines are added to highlight the BPFs.

lower azimuthal orders. The general modal structure does not change dramatically with increasing fan speed. The mode pressure levels are seen to gradually increase from lower to higher fan speeds, with no clear change in structure when passing from subsonic (see approach) to transonic regimes (see sideline), unlike intake mode plots. This might be explained by the fact that shock waves are only present in the intake duct. The effect of aliasing is not clearly seen in this case as compared to the intake mode plots. This is because pressure levels are much lower for modes that are close to the cut-on/cut-off boundary.

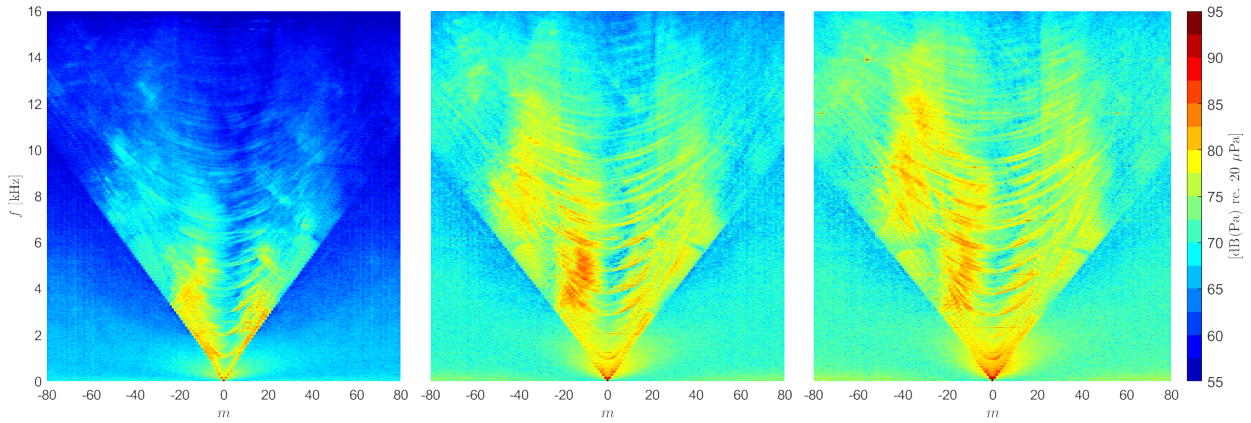

(a) approach (b) cutback (c) sideline

Figure 12: Azimuthal mode detection plots at the bypass duct for three certification points. Results are given for three operating points, namely: (a) approach 50%ND, (b) cutback 80%ND and (c) sideline 90%ND. Results are for the short gap rotor/stator configuration at the sea level static working line (SG-SLSWL). The frequency is plotted against the azimuthal mode order and the modes are coloured by their amplitude.

The azimuthal mode detection maps have been integrated over both co-rotating and counter-rotating modes. Resulting spectra are shown in Fig. 13 at approach and sideline conditions. Compared to intake mode spectra, (see Fig. 11), the levels are more evenly balanced between co-rotating and counter-rotating modes. As frequency increases, however, a trend towards counter-rotating modes is observed for both approach and sideline power. The level difference is on the order of 3 dB. The sketch in Fig. 9 indicates that noise sources located on stator leading edges are likely to favour counter-rotating modes for downstream propagation, since they are more aligned with the dipole suction side lobe. This might explain the predominance of counter-rotating modes. The humps that are observable upstream of the rotor (Fig. 11) do not appear in this downstream section of the duct, which is consistent with their association with inlet duct turbulence proposed in the previous subsection.

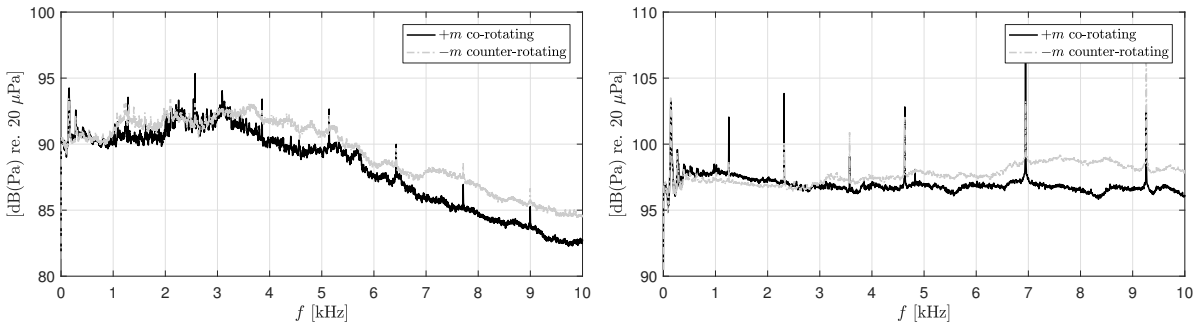

(a) approach (b) sideline

Figure 13: Integrated bypass mode spectra over co-rotating ($+m$) and counter-rotating ($-m$) modes for two fan speeds: (a) approach 50%ND and (b) sideline 90%ND. The results are given for the short fan-OGV gap at the sea level static working line (SG-SLSWL).

4.5. Wavenumber decomposition in the bypass-duct

The test bench is equipped with a linear microphone array in the bypass-duct downstream of the OGV, as outlined in Sec. 3.2. Several post processing techniques can be applied using this kind of array geometry: in-duct beamforming [74, 75] and wavenumber decompositions are common examples [76, 66, 77]. In the present work a wavenumber decomposition is performed through the formulation given by Eq. (7) and solved by iBIA, see Eq. (18). Figure 14 shows the wavenumber domain spectra at different fan speeds, namely: approach, cutback and sideline.

A few remarks are worth noting *prior* to the interpretation of results. First of all, two different features are clearly seen on the 2D wavenumber-frequency plots. The first is a straight line with a low slope that carries high pressure levels at low frequencies. This is associated with the hydrodynamic component and the slope is proportional to the convection velocity of the turbulent structures sweeping past the microphones. An aliasing of the hydrodynamic component onto negative wavenumbers appears when the slope reaches the highest wavenumber resolved by the array which is given by the minimum inter-microphone spacing Δ_z as $k_{z_{max}} = \pi/\Delta_z$. The second region of interest is a "V-shaped" triangle that defines the acoustic domain. Positive wavenumbers k_z are associated with waves propagating downstream and negative wavenumbers with waves propagating upstream. When the aliased hydrodynamic component overlaps the acoustic domain, amplitudes of wavenumber components must be interpreted with care. A second set of aliasing appears when upstream acoustic components are aliased into positive wavenumbers and overlap the acoustic domain. This generally happens at higher frequencies, typically above 10 kHz for the cases analysed in the paper.

The structure of the wavenumber decomposition plots is quite similar for all tested fan speeds, with most energy concentrated in the positive wavenumber domain, that is, sound propagating downstream in the duct. With the exception of very low frequencies, a clear separation between acoustic and hydrodynamic components is obtained. A rippled structure is clearly apparent in the wavenumber-frequency plots, due to amplitude oscillations with frequency. These oscillations can be predicted by the expression of individual mode axial wavenumbers given in Eq. (2), that depends on the frequency. The ripples with larger variations in amplitude that repeat about every 1 kHz correspond to an additional radial order n being cut on in the duct, that produces an accumulation of modes. These are also observed in the bypass azimuthal detection plots from Fig. 12, albeit with a lower dynamic range. Figure 15 provides a deeper analysis by comparing the ripples to the actual cut-on frequencies, see Fig. 15(b). Figure 15(c) displays the cut-on lines only: at low frequency (blue curves below $\approx$ 1 kHz), the azimuthal modes switch on with increasing order m along with increasing frequency, all corresponding to the first radial mode ($n = 0$). At about 1 kHz, the radial mode $n = 1$ switches on (dark orange curves) and intertwines with high azimuthal $n = 0$ modes. This process goes on with more and more radial modes switching on. The difference compared with Fig. 15(a) is that the mode levels are not taken into account in Fig. 15(c).

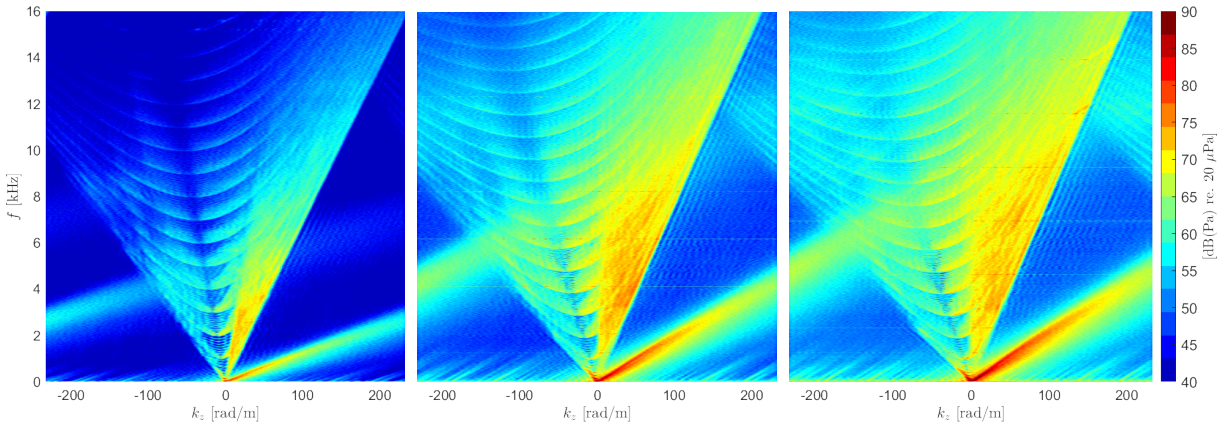

(a) approach (b) cutback (c) sideline

Figure 14: Wavenumber decomposition plots obtained in the bypass-duct for three certification points, namely: (a) approach 50%ND, (b) cutback 80%ND and (c) sideline 90%ND. Results are for the short gap rotor/stator configuration along the sea level static working line (SG-SLSWL). The frequency is plotted against the axial wavenumber and wavenumbers are coloured by their amplitude.

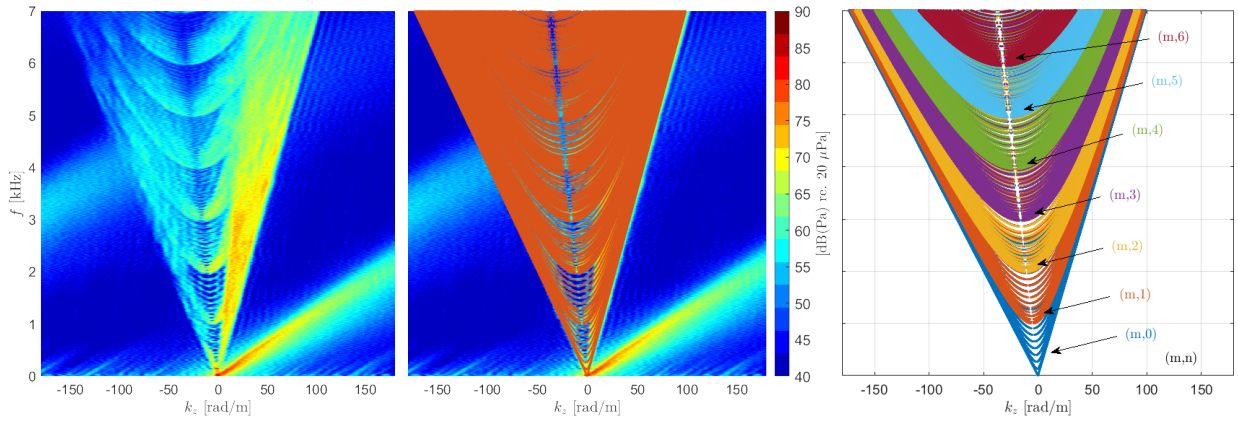

Figure 15: Illustration of the "ripple" structure observed on the wavenumber decomposition plots from Fig. 14. The results of Fig. 14(a) are reproduced for the sake of comparison to theoretical values of mode axial wavenumbers as a function of frequency $k^{\pm}_{z_{m,n}}(\omega)$. The figure shows: (a) same result as Fig. 14(a) with a zoom on both axes for the sake of clarity; (b) same as (a) with the theoretical values of $k^{\pm}_{z_{m,n}}(\omega)$ superposed as red coloured dots. (c) the theoretical values of $k^{\pm}_{z_{m,n}}(\omega)$ are now coloured according to their radial order n.

4.6. Influence of the fan/OGV separation distance

As mentioned in Sec. 3 two different fan-OGV gaps have been tested during the TurboNoiseBB experimental campaign. In this section, a comparison is made between both configurations using in-duct wall-pressure fluctuations data. In particular, the modal content estimated by the different microphone arrays will be used for the analysis. The influence on the noise measured at both intake and bypass-duct is assessed and discussed. It should be kept in mind, however, that the fan was not designed to work for a long-gap associated with the same OGV as that used for the short-gap. In addition a modification of the duct casing has been done for the LG mounting. Thus, the OGV is certainly not operated at the same mean flow conditions for the SG and the LG.

4.6.1. Noise measured at the intake

Azimuthal mode detection plots at the intake measured along the SLSWL for the long-gap (LG) OGV configuration are shown in Fig. 16(a-c). These plots are to be compared to those from the short-gap OGV configuration shown in Fig. 7. A comparison of the LG and SG results reveals that the modal structure is very similar for both configurations. At the approach condition it can be seen that the LG configuration exhibits slightly lower amplitudes than the SG for positive spinning modes, mainly at higher frequencies.

In order to ease the comparison, mode pressure levels are integrated over both co-rotating and counter-rotating mode amplitudes as done in previous sections. Integrated mode spectra at approach are shown in Fig. 17(a). As can be seen, the conclusions differ for co-rotating and counter-rotating mode spectra. For the first, pressure levels for both SG and LG are similar from low frequencies up to 2 kHz. As frequency increases, the LG configuration pressure levels are about 3dB lower than those of the SG configuration. For the counter-rotating pressure spectra, no difference is observed between SG and LG configurations over the whole frequency band. This result suggests that the source mechanism at the origin of this counter-rotating intake noise is not altered by the presence of the stator behind the rotor, as would be the case of rotor interaction with inlet boundary layer. Interestingly the humps found at the intake for the SG also appear for the LG, supporting our assumption that they are related to the structure of the inlet boundary layers. On the other hand, the co-rotating mode spectra suggest that the associated source mechanism is an interaction between fan wakes and OGVs. The results at 60%ND fan speed indicate that the noise reduction of the LG configuration reduces as the fan speed increases. One possible explanation is that the balance between different noise sources is changed with increasing speed.

4.6.2. Noise measured in the bypass duct

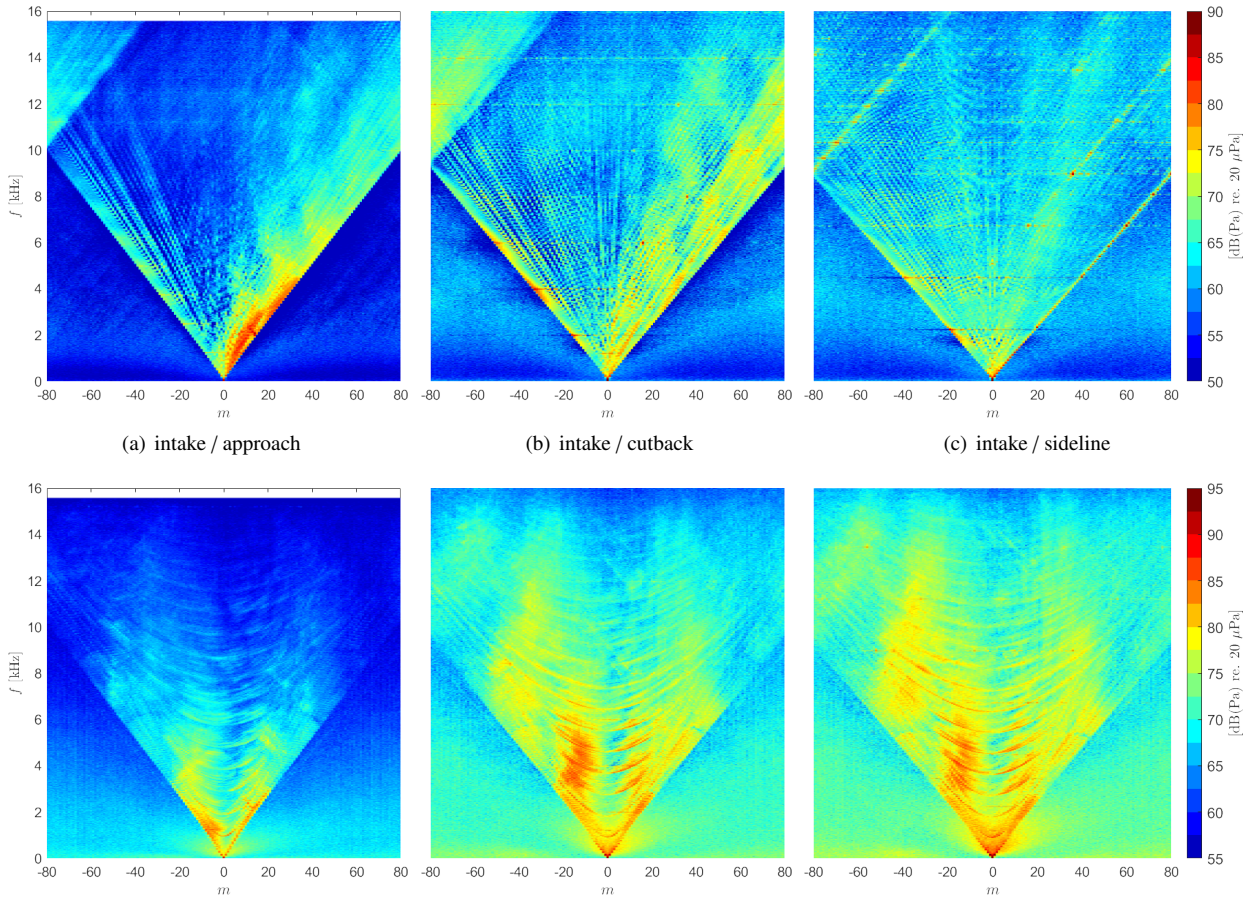

(a) intake / approach (b) intake / cutback (c) intake / sideline

(d) bypass / approach (e) bypass / cutback (f) bypass / sideline

Figure 16: Azimuthal modal distribution for a long-gap OGV configuration. Top row: results in the **intake duct**; Bottom row: results in the **bypass duct**. Mode plots are shown for the three certification fan speeds at the SLS-WL: (a,d) approach 50%ND; (b,e) cutback 80%ND and (c,f) sideline 90%ND. These results are to be compared to those from a short-gap OGV configuration shown respectively in Fig. 7 for the intake duct and in Fig. 12 for the bypass duct.

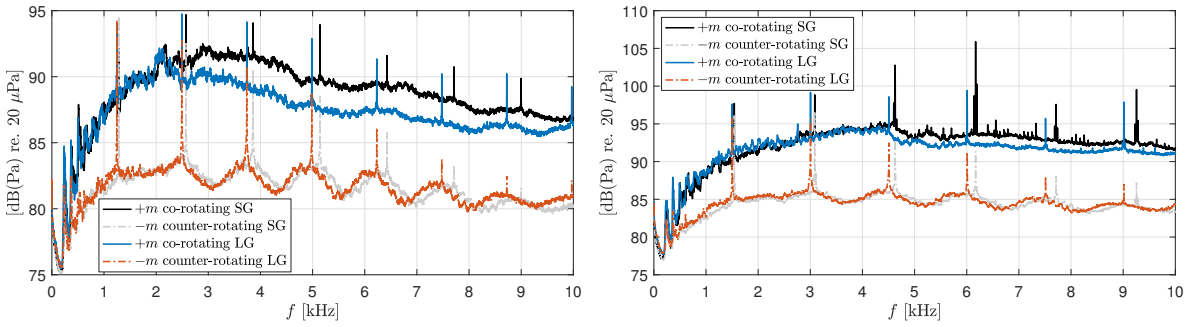

(a) 50%ND (b) 60%ND

Figure 17: Intake mode spectra integrated over co-rotating ($+m$) and counter-rotating ($-m$) modes for both the short-gap and long-gap OGV configurations. Results are shown for two fan speeds: (a) 50%ND and (b) 60%ND.

Azimuthal mode detection plots in the bypass duct for the long-gap OGV configuration are shown in 16(d-f). These results are to be compared to those from a short-gap OGV configuration shown in Fig. 12. As for the intake duct mode distribution, the general structure of the mode-frequency plots is basically the same. Looking at the mode amplitudes for both SG and LG configurations, it can be noticed that the LG configuration shows lower amplitudes at higher frequencies and slightly higher at lower frequencies. As for the intake data, the mode amplitudes are integrated over both co- and counter-rotating modes, allowing for an easier comparison of the two configurations. The results are shown in Fig. 18 for the approach condition. It can be seen that the trends are quite similar for both co-rotating and counter-rotating mode spectra. For the long gap, levels are higher in the low frequency range and lower in the high frequency range than those measured in the short gap configuration. The noise reduction appears to be stronger for counter-rotating modes, see Fig. 18(b). This observation is in agreement with the argument that a larger separation allows for a decrease in the turbulent wake intensity, a widening of wakes and an increase in turbulence length scales. The intensity reduction might explain the observed noise level decrease, whereas the growth of length scales is consistent with the persistent noise level at low frequencies and its reduction at high frequencies.

Additional conclusions can be drawn from Fig. 19 where the noise levels are plotted for the sideline condition (90%ND). In this case the frequency band at which the pressure levels are increased for the LG configuration is even wider, up to about 8 kHz.

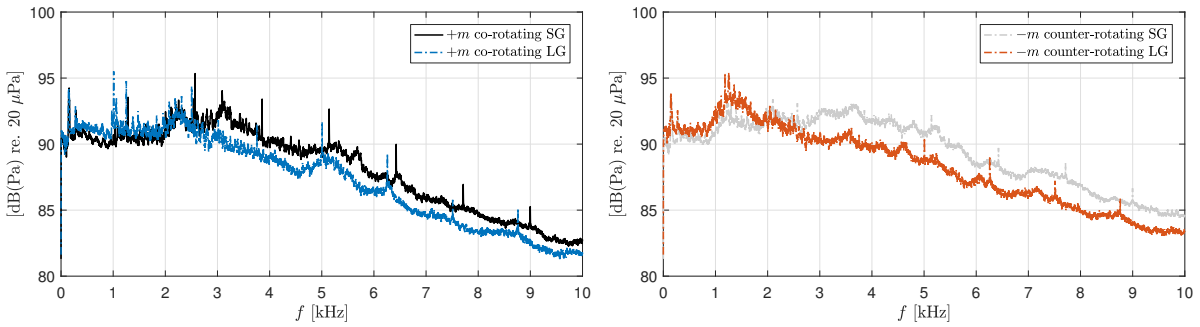

(a) co-rotating (b) counter-rotating

Figure 18: Influence of the fan-OGV separation distance on the noise measured in the bypass duct at approach power. The figure shows integrated mode amplitudes for SG and LG configurations for: (a) co-rotating modes and (b) counter-rotating modes.

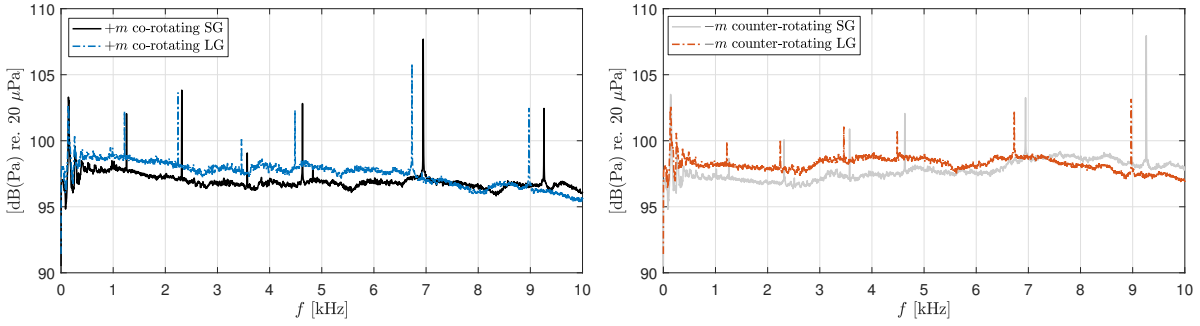

(a) co-rotating (b) counter-rotating

Figure 19: Influence of the fan-OGV separation distance on the noise measured in the bypass duct at sideline power. The figure shows integrated mode amplitudes for SG and LG configurations for: (a) co-rotating modes and (b) counter-rotating modes.

4.7. Estimation of the duct sound power

The decomposition of the in-duct pressure field into azimuthal and radial modes by the ARMD approach (see Eq. (1)), allows for a direct computation of the duct sound power [78]. An illustration of the modal content estimated by this approach using the data from the CMD3 and AX1 microphone arrays is summarized in Fig. 20. A few remarks are worth to mention based on these results: as compared to the azimuthal-only mode detection (AMD), for the ARMD approach, only cut-on modes are taken into account in the model. This can be seen in the results from Fig. 20(a) in the region outside the "modal triangle", in which modes have no amplitude. An interesting feature is that most of the energy is concentrated within a narrower mode "V-shaped" region inside the actual cut-on/cut-off boundary. This can be explained by comparing the theoretical mode cut-off frequencies at both the measurement's annular cross-section where the hub-to-tip ratio is $h = 0.654$ and the stator duct's cross-section where $h = 0.586$. It should be noted that the annular cross-section is constant over the CMD3 and AX1 microphone positions. These mode cut-off frequencies are superimposed on the mode-frequency plot shown in Fig. 20(b) as red and blue dotted lines respectively. It can be seen that the high amplitude region follows the cut-on boundary estimated at the stator duct's cross-section. Modes outside this boundary are cut off by the duct at the stator position and do not propagate up to the actual measurement section, where CMD3 and AX1 microphones are located. In addition, the azimuthal mode cut-off frequencies for the radial $n = 3$ mode are also superimposed on the mode-frequency plot as black dots. This illustrates that the mode hyperbolas correspond to higher radial orders being cut-on in the duct, as the results of the wavenumber decomposition, see Fig. 15. These results compare to those from Fig. 16(e) obtained from the AMD approach using only data from the CMD3 circular ring. However, it should be pointed out that the ARMD results are given only up to the frequency of 10 kHz since the condition number of the modal basis associated with the matrix $\mathbf{\Phi}$ was too high for higher frequencies. Finally, an example of the complete breakdown into azimuthal and radial mode amplitudes $A^{+}_{m,n}$ obtained by the ARMD approach is shown in Fig. 20(c). The results shown for the 3150 Hz third-octave band are obtained by summing over the narrow-band analyses. Notice that as the radial order increases, the number of cut-on azimuthal orders is reduced. Once the set of $A^{\pm}_{m,n}$ amplitudes are estimated, the individual mode sound power $W^{\pm}_{m,n}$ is easily computed through the following equation:

$$W^{\pm}_{m,n} = \frac{k_0 S \beta^4}{2Z_0} \frac{\hat{k}_{r_{m,n}}}{\left(k_0 \mp M_z \hat{k}_{r_{m,n}}\right)^2} \left|A^{\pm}_{m,n}\right|^2, \tag{23}$$

with $S = \pi(r_t^2 - r_h^2)$ being the duct cross-section surface at the mode detection plane in the bypass duct, $Z_0 = \rho_0 c$ is the acoustic impedance and $\hat{k}_{r_{m,n}}$ is given by Eq. (3). Equation (23) gives the sound power $W_{m,n}$ radiated by each individual mode of azimuthal order m and radial order n. The total transmitted sound power along the duct can be obtained by summing Eq. (23) over all azimuthal and radial mode orders. It provides the total in-duct sound power transmitted either downstream W^{+} or upstream W^{-}:

$$W^{\pm} = \frac{k_0 S \beta^4}{2Z_0} \sum_{m=-M}^{M} \sum_{n=0}^{N} \frac{\hat{k}_{r_{m,n}}}{\left(k_0 \mp M_z \hat{k}_{r_{m,n}}\right)^2} \left|A^{\pm}_{m,n}\right|^2, \tag{24}$$

where M and N are respectively the maximum azimuthal and radial orders reached by cut-on modes at each angular frequency ω. Often it is not possible to obtain a complete modal breakdown since it requires a relatively large number of microphones distributed over azimuthal and axial positions. It is of interest thus to obtain an estimate of the in-duct sound power based on simplified analyses such as azimuthal mode detection (AMD) or wavenumber decompositions (WND). However, this requires an assumption regarding the distribution of the modal energy over the radial and/or azimuthal modes. This was investigated by Joseph et al. [79], where different assumptions about the modal distribution were studied. In the present work, two assumptions often used for the modelling of fan broadband noise are tested. The first one assumes an equal energy per mode (EEpM) and the second one an equal energy density per mode (EEDpM). The expressions leading to the duct sound power based on either WND or AMD combined with the two mode distributions are given in Appendix C. It is worth noting that for the WND based approach, the assumption covers both the azimuthal and radial modes. However for the AMD based approach, the assumption is only made for the radial modes, the azimuthal amplitudes are given by the mode detection approach. The duct sound power estimate given by the azimuthal and radial mode decomposition (ARMD), see Eq. (24), is now compared to estimates issued from an azimuthal only (AMD) and wavenumber decompositions (WND).

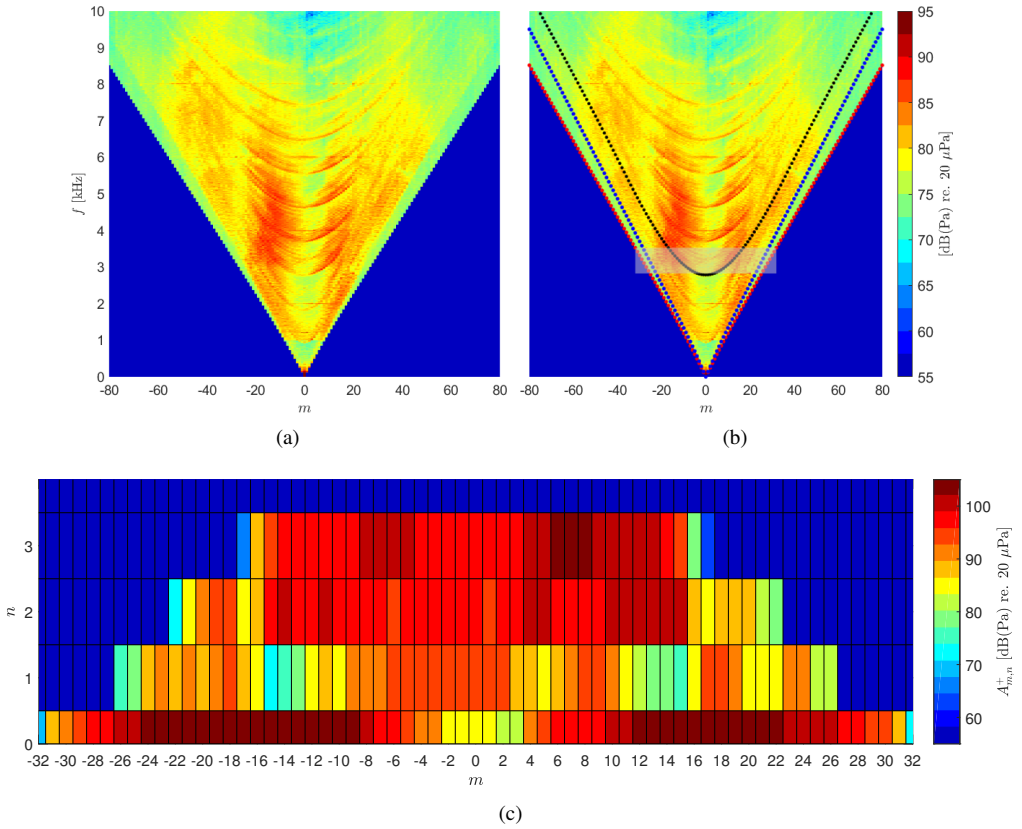

Figure 20: Example of the azimuthal and radial modal content as obtained by the ARMD approach using the data from both CMD3 and AX1 arrays. Results are given for the cutback 80%ND operating point and the long gap rotor/stator configuration along the sea level static working line (LG-SLSWL). (a) Azimuthal mode distribution as a function of frequency considering the contribution from all cut-on radial orders. (b) The same result as (a) with the theoretical mode cut-off frequencies superimposed onto the plot. The red dots are mode cut-off frequencies computed at the CMD3AX1 axial section with hub-to-tip ratio $h = 0.654$. The blued dots are cut-off frequencies computed at the stator axial section with $h = 0.586$. The black dots are mode cut-off frequencies for azimuthal modes at a fixed $n = 3$ radial order, that is, $A_{m,3}$. The light grey box corresponds to the frequency band for which the azimuthal and radial mode distribution is shown in (c). (c) Complete mode breakdown showing the amplitudes of both azimuthal and radial modes propagating downstream in the duct $A^+_{m,n}$.

First of all, the assumptions of EEpM and EEDpM are combined to both WND and AMD approaches to obtain sound power estimates to be compared to those from Eq. (24) with $A^{\pm}_{m,n}$ estimated by the ARMD approach. The results are shown in Fig. 21 for measured data at the approach condition and the short-gap OGV configuration. It can be seen that the EEpM assumption combined with WND produces an oscillatory behaviour with the frequency that is not observed on the sound power estimates based for the ARMD approach. The oscillations have also been noted by Joseph et al. [79] and the dips in the response coincide with frequencies approaching the mode cut-off frequencies. The sound power estimates with WND using the EEDpM assumption do not show the dips. The comparison of WND estimates with both EEpM and EEDpM to those from ARMD shows that the power levels better match the equal energy per mode model, however the frequency shape following more the equal energy density per mode (that is, without the dips in the spectrum). The differences between EEpM and EEDpM sound power estimates are rather small, on the order of 2 dB. Figure 21(b) compares the two assumptions combined with the AMD mode amplitude estimations. It can be seen that sound power estimates based on both EEpM and EEDpM are very similar when coupled to the AMD results. It should be noted that in this case the assumption is made on the radial mode distribution.

The comparison of sound power estimates at cutback and sideline are shown in Fig. 22. Similar trends as for the approach case are observed. At low frequencies up to 1 kHz the AMD based estimates are a few dB higher than others. The fact that AMD does not distinguish the upstream and downstream modes is likely to be the cause.

Indeed, considering the wavenumber-frequency plots in Fig. 14, in which it can be seen for frequencies below 1 kHz that upstream waves (negative k_z) show quite large amplitudes as compared to downstream ones. Similarly to the approach case, WND coupled with the EEpM assumption gives sound power levels that better match those from ARMD, although the correct frequency shape rather followed by the EEDpM assumption.

Finally, a few remarks are worth to mention. Since the ARMD sound power estimates do not require any assumption on the modal distribution, they are taken here as the reference for the comparison. Uncertainties on the ARMD are not expected to be larger than for the AMD and the WND for the reasons detailed hereafter. Indeed, uncertainties are due either to the approximation of physical parameters (sound speed, mean flow velocity or plug flow assumption) or to the regularisation. In both cases the uncertainties are expected to be of the same order for the three approaches. Moreover, if the uncertainties lead to a significant effect, they would have a stronger impact on the higher frequencies and the tones as the modal distribution is a consequence of interferences that are sensitive to phase errors. Tones are not in the scope of the present study and Figs. 21 and 22 show that the broadband sound power spectra differ mostly in the low frequency range (below 1 kHz).

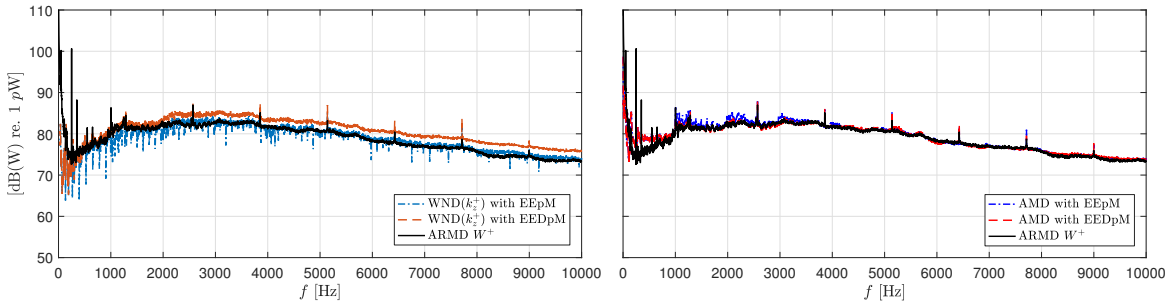

(a) (b)

Figure 21: Comparison between different estimates of the in-duct sound power in the bypass duct. ARMD: Azimuthal and Radial Modal Decomposition, WND: Wavenumber Decomposition and AMD: Azimuthal Modal Decomposition. The results compare the sound power estimate given by the ARMD to those from WND and AMD based on two assumptions: equal energy per mode (EEpM) and equal energy density per mode (EEDpM). Results are given for the sea level static working line and for the short-gap OGV configuration (SG-SLSWL) at approach 50%ND: (a) Based on wavenumber decomposition and (b) Based on azimuthal mode decomposition.

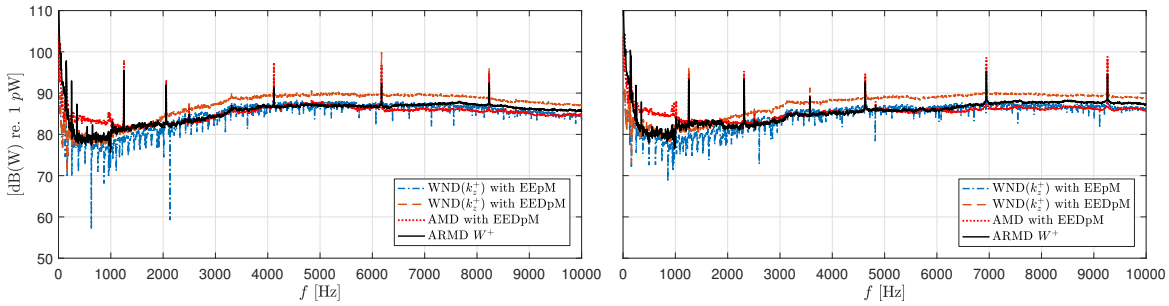

(a) cutback (b) sideline

Figure 22: Comparison between different estimates of the in-duct sound power at the bypass-duct for two operating points (a) cutback 80%ND and (b) sideline 90%ND. ARMD: Azimuthal and Radial Modal Decomposition, WND: Wavenumber Decomposition and AMD: Azimuthal Modal Decomposition. Results are given for the sea level static working line and for the short-gap OGV configuration (SG-SLSWL).

5. Conclusions

Fan broadband noise is responsible for a major part of aircraft overall noise for future UHBR engine architectures. To improve understanding of its generation mechanisms an extensive experimental database has been acquired within

the TurboNoiseBB project. The present work has been focused on the analysis of broadband noise at both the intake duct and the bypass section of a rotor/stator stage.

Azimuthal mode detection (AMD) and wavenumber decomposition (WND) of wall-pressure fluctuations data have been computed from the dataset. The application of an iterative Bayesian Inverse Approach (iBIA) provided results with improved dynamic range and limited aliasing when compared to two classical approaches, namely Least-Squares Beamforming and an inverse method. The possibility of setting a parameter controlling the sparsity degree makes this approach interesting enough to be applied to both broadband and tonal fan noise. In this work, as fan broadband noise was of main interest, a mild sparsity assumption has been used. Another interesting point of iBIA is that the regularisation procedure for the inverse computation is fully automated and estimated from the data. In addition the method is applied directly to the cross-spectral matrix of measurements, taking advantage of averaging the data over several time snapshots whenever the measured signals are assumed stationary and ergodic.

A short-gap (SG) and a long-gap (LG) OGV configuration have been compared in terms of the noise generated both at the intake and at the bypass. Increasing the rotor-stator spacing has shown reduced levels at higher frequencies for intermediate fan speeds (see approach) for both inlet and exhaust noise. With increasing fan speed the difference between SG and LG configurations tends to decrease and the LG even reaches higher levels for exhaust noise at low frequencies. However, it is important to mention that the fan was not designed to work for an LG associated with the same OGV as that used for the SG. In addition a modification of the duct casing has been done for the LG mounting. For all these reasons, the OGV is certainly not operated at the same mean flow conditions for the SG and the LG.

The in-duct sound power has been estimated through three different approaches. One based on a complete azimuthal and radial (ARMD) modal breakdown and two that require further assumptions about the modal distribution. Two assumptions commonly used for the modelling of fan broadband noise have been evaluated: an equal energy per mode (EEpM) distribution and an equal energy density per mode (EEDpM) distribution. The sound power estimates based on the AMD tend to over predict the levels at very low frequencies and are seen not to significantly depend on the choice of either EEpM or EEDpM assumptions. The over-predictions at low frequencies are likely due to the lack of separation between downstream and upstream modes, the latter being non-negligible at those frequencies for the test bench used in the experimental set-up. Conversely, the WND associated with both EEDpM and EEpM leads to better estimates at low frequencies due to the separation between downstream and upstream waves. The WND associated with EEDpM overpredicts the sound power levels by about 3 dB in the higher frequency range, contrary to its association with EEpM. Thus the ARMD method described in the present paper was successfully applied to assess the widely used EEpM and EEDpM assumptions.

Acknowledgements

The presented work was conducted in the frame of the project TurboNoiseBB, which has received funding from the European Union's Horizon 2020 research and innovation program under grant agreement No. 690714. It was also performed within the framework of the industrial chair ARENA (ANR-18-CHIN-0004-01) co-financed by Safran Aircraft Engines and the French National Research Agency (ANR) and in the framework of the Labex CeLyA (ANR-10-LABX-0060) of the Université de Lyon, within the program "Investissements d'Avenir" (ANR-16-IDEX-0005) operated by the French National Research Agency (ANR).

The authors kindly acknowledge: all the team from TurboNoiseBB involved in the test campaign, Professor Michel Roger for several discussions on the interpretation of experimental results and the two anonymous reviewers for their careful reading and pertinent comments.

Appendix A. Computation of radial wavenumbers for rigid walled cylindrical ducts

Appendix A.1. Annular cross section

The radial shape factor $f_{m,n}(r)$ in Eq. (1), which is a solution of the Bessel equation for an annular cylindrical duct, writes

$$f_{m,n}(r) \propto C_{1_{m,n}} J_{|m|}(k_{r_{m,n}} r) + C_{2_{m,n}} Y_{|m|}(k_{r_{m,n}} r), \tag{A.1}$$

where J_m is the m-th order Bessel function of first type and Y_m the m-th order Bessel of second type (or Neumann function) while $C_{1_{m,n}}$, $C_{2_{m,n}}$ and $k_{r_{m,n}}$ are coefficients determined by boundary conditions. The proportional sign is used

to emphasize that the $f_{m,n}(r)$ is defined up to a constant multiplicative factor, that is introduced in the next section such as to ensure its normalisation. The radial wavenumber $k_{r_{m,n}}$ is obtained through the wall boundary conditions at the outer radius noted here as $r = r_t$ and the inner radius as $r = r_h$. Considering the case of hard wall boundaries, the following conditions must be met

$$\frac{\partial \hat{p}(z,r,\phi)}{\partial r}\Big|_{r=r_t} = 0 \quad \text{and} \quad \frac{\partial \hat{p}(z,r,\phi)}{\partial r}\Big|_{r=r_h} = 0, \tag{A.2}$$

which then leads to the following system of equations

$$\begin{bmatrix} J'_{|m|}(k_{r_{m,n}} r_t) & Y'_{|m|}(k_{r_{m,n}} r_t) \\ J'_{|m|}(k_{r_{m,n}} r_h) & Y'_{|m|}(k_{r_{m,n}} r_h) \end{bmatrix} \times \begin{pmatrix} C_{1_{m,n}} \\ C_{2_{m,n}} \end{pmatrix} = \begin{pmatrix} 0 \\ 0 \end{pmatrix}. \tag{A.3}$$

Thus, the set of two homogeneous boundary conditions may be used to determine $k_{r_{m,n}}$ and the ratio $C_{1_{m,n}}/C_{2_{m,n}}$. Setting the determinant to zero, the radial wavenumber $k_{r_{m,n}}$ is obtained from

$$J'_{|m|}(k_{r_{m,n}} r_t) Y'_{|m|}(k_{r_{m,n}} r_h) - J'_{|m|}(k_{r_{m,n}} r_h) Y'_{|m|}(k_{r_{m,n}} r_t) = 0, \tag{A.4}$$

which can be rewritten by introducing the following variables

$$h = \frac{r_h}{r_t} \quad \text{and} \quad \lambda_{m,n} = k_{r_{m,n}} r_t, \tag{A.5}$$

where h is the hub-to-tip ratio. Equation (A.4) is then rewritten as

$$J'_{|m|}(\lambda_{m,n}) Y'_{|m|}(\lambda_{m,n} h) - J'_{|m|}(\lambda_{m,n} h) Y'_{|m|}(\lambda_{m,n}) = 0. \tag{A.6}$$

The n-th root $\lambda_{m,n}$ of this equation yields the radial wavenumber by the following relation

$$k_{r_{m,n}} = \frac{\lambda_{m,n}}{r_t}. \tag{A.7}$$

It should be pointed out that the eigenvalues $\lambda_{m,n}$ are given for a fixed hub-to-tip ratio h. This means that the cut-off frequency varies along with the duct cross-section, explaining why some modes may switch from cut-on to cut-off or *vice-versa* as they propagate through the duct. The roots of Eq. (A.6) can be found numerically. The constants $C_{1_{m,n}}$ and $C_{2_{m,n}}$ may be determined by Eq. (A.3) only up to an arbitrary multiplicative factor. Setting $C_{m,n} = C_{2_{m,n}}/C_{1_{m,n}}$ and $C_{1_{m,n}} = 1$, Eq. (A.1) can be written as

$$f_{m,n}(r) \propto J_{|m|}(k_{r_{m,n}} r) + C_{m,n} Y_{|m|}(k_{r_{m,n}} r), \tag{A.8}$$

where the value of $C_{m,n}$ is obtained from Eq. (A.3) and is written

$$C_{m,n} = -\frac{J'_{|m|}(k_{r_{m,n}} r_t)}{Y'_{|m|}(k_{r_{m,n}} r_t)}. \tag{A.9}$$

The radial shape factor is finally defined as

$$f_{m,n}(r) = \frac{1}{\Gamma_{m,n}} \left(J_{|m|}(k_{r_{m,n}} r) + C_{m,n} Y_{|m|}(k_{r_{m,n}} r) \right), \tag{A.10}$$

where the normalisation factor $\Gamma_{m,n}$ is to be defined such as to satisfy the normalisation condition given in Appendix B.

Appendix A.2. Circular cross section

For a duct with circular cross section, the acoustic pressure must be finite when r tends to zero. Thus, the coefficient $C_{2_{m,n}}$ in Eq. (A.1) must be zero, since the Neumann function tends to $-\infty$ at $r = 0$. The radial shape factor $f_{m,n}(r)$ thus is written

$$f_{m,n}(r) = \frac{J_{|m|}(k_{r_{m,n}} r)}{\Gamma_{m,n}}. \tag{A.11}$$

If one assumes a hard-wall condition, that is, that the particle velocity or the derivative of the acoustic pressure with respect to r is zero, the following condition must be fulfilled:

$$J'_{|m|}(\kappa_{m,n}) = J'_{|m|}(k_{r_{m,n}} r_t) = 0, \tag{A.12}$$

with $J'_{|m|}(\cdot)$ the first derivative of the mth order Bessel function $J_{|m|}(\cdot)$ and r_t the duct casing radius. Note that $\kappa_{m,n}$ is the eigenvalue for a dimensionless radius or $r_t = 1$. For any particular value of azimuthal order $|m|$, the n-th root $\kappa_{m,n}$ of $J'_{|m|}(\kappa_{m,n}) = 0$ gives the radial wavenumber:

$$k_{r_{m,n}} = \frac{\kappa_{m,n}}{r_t}. \tag{A.13}$$

Appendix B. Normalisation constant

The goal is to ensure that the modal functions in Eq. (1) are normalised over the duct's surface. This is mathematically written through the following general assumption:

$$\frac{1}{S} \int_S \phi_i(x, y) \phi_j^*(x, y) dS = \delta_{ij}, \tag{B.1}$$

that is, the integral over a duct's cross section S of the product of two functions ϕ_i and ϕ_j is equal to the Kronecker delta function. Note that the space variables x and y are set according to the coordinate system defined in Fig. 1.

Appendix B.1. Annular cross-section

For convenience when dealing with a circular or annular duct cross-section the polar coordinates r and θ are preferred. For an annular cross-section the following definition is made for the sake of simplicity:

$$\mathbb{S}_{|m|}(k_{r_{m,n}} r) = J_{|m|}(k_{r_{m,n}} r) + C_{m,n} Y_{|m|}(k_{r_{m,n}} r), \tag{B.2}$$

thus Eq. (B.1) reads

$$\frac{1}{\pi(r_t^2 - r_b^2)} \int_{r_h}^{r_t} \int_0^{2\pi} \frac{\mathbb{S}^2_{|m|}(k_{r,m,n} r)}{\left|\Gamma_{m,n}\right|^2} d\theta r dr = 1, \tag{B.3}$$

that gives a normalisation constant in the form of

$$\left|\Gamma_{m,n}\right|^2 = \frac{1}{\pi(r_t^2 - r_h^2)} \int_{r_h}^{r_t} \int_0^{2\pi} \mathbb{S}^2_{|m|}(k_{r_{m,n}} r) d\theta r dr. \tag{B.4}$$

The integral over r in the right hand side of Eq. (B.4) is recognised as a Lommel's integral [80] and its solution is explicitly found in mathematical textbooks [80]:

$$\int_{r_h}^{r_t} \mathbb{S}^2_{|m|}(k_{r_{m,n}} r) r dr = \left[\frac{r^2}{2} \left\{ \left(1 - \frac{m^2}{(k_{r_{m,n}} r)^2} \right) \mathbb{S}^2_{|m|}(k_{r_{m,n}} r) \right\} \right]_{r_h}^{r_t}, \tag{B.5}$$

which then leads to the following squared normalisation constant

$$\left|\Gamma_{m,n}\right|^2 = \frac{1}{\cancel{\pi}(r_t^2 - r_h^2)} \frac{\cancel{2}\pi}{\cancel{2}} \left[r^2 \left\{ \left(1 - \frac{m^2}{(k_{r_{m,n}} r)^2} \right) \mathbb{S}^2_{|m|}(k_{r_{m,n}} r) \right\} \right]_{r_h}^{r_t}, \tag{B.6}$$

that finally leads to the normalisation constant

$$\Gamma_{m,n} = \sqrt{\frac{1}{(r_t^2 - r_h^2)} \left[r^2 \left\{ \left(1 - \frac{m^2}{(k_{r_{m,n}} r)^2} \right) \mathbb{S}^2_{|m|}(k_{r_{m,n}} r) \right\} \right]_{r_h}^{r_t}}, \tag{B.7}$$

Appendix B.2. Circular cross-section

For a circular duct, using the modal shape factor $f_{m,n}(r)$ from Eq. (A.11) leads to the following integral:

$$\frac{1}{\pi r_t^2}\int_0^{r_t}\int_0^{2\pi}\frac{J_{|m|}^2(k_{r_{m,n}}r)}{\left|\Gamma_{m,n}\right|^2}d\theta r dr = 1. \tag{B.8}$$

It is indeed readily deduced from (B.7) by setting $r_h = 0$ and $C_{m,n} = 0$ in $\mathbb{S}_{|m|}$. The normalisation factor thus writes

$$\Gamma_{m,n} = \sqrt{\left(1-\frac{m^2}{(k_{r_{m,n}}r_t)^2}\right)J_{|m|}^2(k_{r_{m,n}}r_t)}. \tag{B.9}$$

Appendix C. Expressions for the computation of the transmitted duct sound power

Joseph *et al.* [79] presented an extensive analysis of sound power transmission in ducts with flow. In particular, an expression that relates the averaged-pressure at the duct wall to the transmitted sound power was derived. This relation was also estimated for different assumptions on the modal distributions such as equal energy per mode (EEpM), equal energy density per mode (EEDpM), a uniform distribution of incoherent monopoles and a uniform distribution of incoherent axial dipoles. The derivations are not shown here for the sake of brevity and the reader is referred to ref. [79] for further details. Of particular interest for the present work are both the assumptions of equal energy per mode and equal energy density per mode which are commonly used for modelling broadband noise. The first assumes that all modes carry equal power and is defined by setting $W_{m,n} = \bar{W}$, with $\bar{W}$ a constant. The second assumes that each mode produces the same spatial energy density or energy per unit volume $E_{m,n}$, that is defined as:

$$E_{m,n} = \frac{W_{m,n}}{S\,c_{g_{m,n}}} = E, \tag{C.1}$$

where S is the duct cross-section surface, E is a constant and $c_{g_{m,n}}$ is the modal axial group velocity which is given by

$$c_{g_{m,n}} = \frac{1}{dk_{z_{m,n}}/d\omega}. \tag{C.2}$$

Note that $E_{m,n}$ is a density in space, not an energy density in frequency (*i.e.* not a spectral density). The two assumptions are worked out to be used along with experimental data issued from a wavenumber decomposition as well as an azimuthal mode decomposition, in order to estimate the sound power. This is detailed in the next sub-sections.

Appendix C.1. Sound power estimate based on the wavenumber-filtered wall-pressure fluctuations

From Eqs. (20b), (22), (38) and (39) of ref. [79] it can be shown that assuming an EEDpM distribution the sound power transmitted either downstream (W^+) or upstream (W^-) in a duct with flow can be written as a function of the averaged pressure at the duct wall as

$$W^{\pm}_{\mathrm{EEDpM}} = \left(\frac{\mathbf{p}^H\mathbf{p}}{K}\right)\frac{S\beta^4}{\rho_0 c}\frac{\sum_m\sum_n \alpha_{m,n}\left(1\mp\alpha_{m,n}M_z\right)^{-1}}{\sum_m\sum_n\left(1\mp\alpha_{m,n}M_z\right)f_{m,n}^2(r_t)}, \tag{C.3}$$

where S is the surface of the duct cross-section, β the Prandtl-Glauert factor, K the number of microphones the pressure signals of which are averaged and $\alpha_{m,n}$ is defined as the cut-on ratio of each individual mode. Note that the assumption of equal energy density per mode was made to derive this expression. The first term on the right-hand side represents the average of pressure fluctuations over a set of microphones at the duct wall. The modal cut-on ratio is defined as

$$\alpha_{m,n} = \frac{\hat{k}_{r_{m,n}}}{k_0}, \tag{C.4}$$

in terms of the modified radial wavenumber $\hat{k}_{r_{m,n}}$ given in Eq. (3). Using Eq. (2) the modal cut-on ratio can be also expressed as a function of the mode axial wavenumber $k_{z_{m,n}}$:

$$\pm\alpha_{m,n} = \beta^2 \frac{k^{\pm}_{z_{m,n}}}{k_0} + M_z \tag{C.5}$$

Similarly, by using Eq. (3) it can be equivalently written as a function of the mode radial wavenumber $k_{r_{m,n}}$:

$$\alpha_{m,n} = \sqrt{1 - \beta^2 \left(\frac{k_{r_{m,n}}}{k_0}\right)^2}. \tag{C.6}$$

Equation (C.4) is particularly useful to rewrite the expression of the individual modal sound power from Eq. (23) as a function of the modal cut-on ratio, as commonly found in the literature [78, 79]:

$$W^{\pm}_{mn} = \frac{S\beta^4}{2Z_0} \frac{\alpha_{m,n}}{(1 \mp M_z\alpha_{m,n})^2} \left|A^{\pm}_{m,n}\right|^2. \tag{C.7}$$

The assumption of an equal energy per mode (EEpM) distribution leads to the following expression for the transmitted sound power

$$W^{\pm}_{\mathrm{EEpM}} = \left(\frac{\mathbf{p}^H\mathbf{p}}{K}\right) \frac{S\beta^4}{\rho_0 c} \frac{N_c^{(m,n)}(\omega, M_z)}{\sum_m \sum_n \alpha^{-1}_{m,n} (1 \mp \alpha_{m,n}M_z)^2 f^2_{m,n}(r_t)}, \tag{C.8}$$

where $N_c^{(m,n)}(\omega, M_z)$ is the number of cut-on modes whose dependence on the frequency ω and the Mach number M_z is made explicit.

The vector $\mathbf{p} \in \mathbb{C}^K$ in Eqs. (C.3) and (C.8) stands for the pressure fluctuations measured at a set of K microphone positions. One approach consists in using the overall wall-pressure fluctuations sensed by the microphones. However, it is known that the broadband content of wall-pressure fluctuations is dominated by hydrodynamic components due to the turbulent boundary layer. Thus, a strong bias on the estimated sound power is expected if Eq. (C.3) is directly applied to measured wall-pressure fluctuations. The wavenumber decomposition shown in Sec. 4.5 provides a convenient way to filter out different contributions from the total measured wall-pressure fluctuations. Of particular interest here are positive wavenumbers k_z^+ within the acoustic domain that describe downstream propagating sound, see Fig. 14. Once the wavenumber coefficients D_{k_z} are estimated by Eq. (18), a new vector of filtered pressure fluctuations $\mathbf{p}_{(k_z^+)}$ can be obtained by truncating the sum in Eq. (7) to positive k_z in the acoustic domain and evaluating for all axial microphone positions z. The vector $\mathbf{p}_{(k_z^+)}$ is then used as input to the Eqs. (C.3) and (C.8).

Appendix C.2. Sound power estimate based on the azimuthal-only mode decomposition

The estimation of azimuthal mode amplitudes such as given by microphones distributed over the duct circumference, does not allow the direct computation of the transmitted sound power, as it does with Eq. (24). However, an approximation might be done if assumptions are made about the modal energy distribution. As in the previous sub-section the assumptions of equal energy per mode and equal energy density per mode are evaluated. Following the same procedure as above, an estimate of the sound power carried by each azimuthal mode m assuming an EEDpM distribution is computed by

$$W^{\pm}_{m_{(EEDpM)}} = \frac{S\beta^4}{\rho_0 c} \frac{\sum_n \alpha_{m,n} (1 \mp \alpha_{m,n}M_z)^{-1}}{\sum_n (1 \mp \alpha_{m,n}M_z) f^2_{m,n}(r_0)} \left|C_m(z_0, r_0)\right|^2, \tag{C.9}$$

where $C_m(z_0, r_0)$ is the azimuthal amplitude of the mode m estimated at the axial position z_0 and radial position r_0. In the present work $r_0 = r_t$ since the microphone ring is located at the duct outer casing. It is important to keep in mind that the mode amplitude estimated with a single ring of microphones does not separate downstream C_m^+ and upstream C_m^- propagating modes. Thus, Eq. (C.9) is expected to be a rough estimate of the actual duct sound power when both components have non negligible amplitudes. In the present case the wavenumber decomposition in Fig. 14 shows that upstream propagating waves are observed (see negative k_z components), although with lower amplitudes

as compared to downstream propagating sound (positive k_z). Thus, it is expected that $C_m(z_0, r_0)$ in Eq. (C.9) is dominated by downstream modes C_m^+. The following expression gives the azimuthal mode sound power assuming a EEpM distribution:

$$W^{\pm}_{m_{(EEpM)}} = \frac{S\beta^4}{\rho_0 c} \frac{N_c^{(n)}(\omega, M_z)}{\sum_n \alpha_{m,n}^{-1} \left(1 \mp \alpha_{m,n} M_z\right)^2 f_{m,n}^2(r_t)} \left|C_m(z_0, r_0)\right|^2 , \tag{C.10}$$

where $N_c^{(n)}(\omega, M_z)$ is the number of cut-on radial orders with respect to the azimuthal mode m.

Finally, the total transmitted sound power can be directly computed as

$$W^{\pm} = \sum_m W_m^{\pm}. \tag{C.11}$$

References

[1] https://www.acare4europe.org/sria/flightpath-2050-goals/protecting-environment-and-energy-supply-0, accessed: 2021-02-25.

[2] https://www.dlr.de/at/desktopdefault.aspx/tabid-12815/22389_read-53176/, accessed: 2021-02-25.

[3] B. Mugridge, The measurement of spinning acoustic modes generated in an axial flow fan, Journal of Sound and Vibration 10 (2) (1969) 227–246. doi:10.1016/0022-460x(69)90198-9.

[4] U. Bolleter, M. J. Crocker, Theory and measurement of modal spectra in hard-walled cylindrical ducts, The Journal of the Acoustical Society of America 51 (5A) (1972) 1439–1447. doi:10.1121/1.1912994.

[5] P. Harel, M. Perulli, Measurement, in a duct, of the space-structure of the discrete-frequency noise generated by an axial compressor, Journal of Sound and Vibration 23 (4) (1972) 487–506. doi:10.1016/0022-460x(72)90505-6.

[6] G. F. Pickett, T. G. Sofrin, R. A. Wells, Method of fan sound mode structure determination, Tech. rep., NASA CR-135293 (1977).

[7] C. Moore, Measurement of radial and circumferential modes in annular and circular fan ducts, Journal of Sound and Vibration 62 (2) (1979) 235 – 256.

[8] L. Enghardt, Y. Zhang, W. Neise, Experimental verification of a radial mode analysis technique using wall-flush mounted sensors, The Journal of the Acoustical Society of America 105 (2) (1999) 1186–1186. doi:10.1121/1.425598.

[9] D. Hall, L. Heidelberg, K. Konno, Acoustic mode measurements in the inlet of a model turbofan using a continuously rotating rake - data collection/analysis techniques, in: 31st Aerospace Sciences Meeting, American Institute of Aeronautics and Astronautics, 1993. doi:10.2514/6.1993-599.

[10] L. Heidelberg, D. Hall, Acoustic mode measurements in the inlet of a model turbofan using a continuously rotating rake, in: 31st Aerospace Sciences Meeting, American Institute of Aeronautics and Astronautics, 1993. doi:10.2514/6.1993-598.

[11] D. L. Sutliff, Turbofan duct mode measurements using a continuously rotating microphone rake, International Journal of Aeroacoustics 6 (2) (2007) 147–170. doi:10.1260/147547207781041859.

[12] P. Sijtsma, H. Orsi, Azimuthal and radial mode detection by a slowly rotating rake, in: 19th AIAA/CEAS Aeroacoustics Conference, American Institute of Aeronautics and Astronautics, 2013. doi:10.2514/6.2013-2244.

[13] L. Enghardt, L. Neuhaus, C. Lowis, Broadband sound power determination in flow ducts, in: 10th AIAA/CEAS Aeroacoustics Conference, no. 2940, 2004.

[14] A. Pereira, J. Regnard, E. Salze, F. Gea-Aguilera, M. Gruber, New modular fan rig for advanced aeroacoustic tests - modal decomposition on a 20" UHBR fan stage, in: Proceedings of the 25th AIAA/CEAS Aeroacoustics Conference, Delft, Netherlands, AIAA Paper 2019-2604, 2019.

[15] P. D. Joppa, An acoustic mode measurement technique, in: 9th Aeroacoustics Conference, American Institute of Aeronautics and Astronautics, 1984. doi:10.2514/6.1984-2337.

[16] P. D. Joppa, Acoustic mode measurements in the inlet of a turbofan engine, Journal of Aircraft 24 (9) (1987) 587–593. doi:10.2514/3.45482.

[17] S. Sarin, E. Rademaker, In-flight acoustic mode measurements in the turbofan engine inlet of fokker 100 aircraft, in: 15th Aeroacoustics Conference, American Institute of Aeronautics and Astronautics, 1993. doi:10.2514/6.1993-4414.

[18] E. Rademaker, P. Sijtsma, B. Tester, Mode detection with an optimised array in a model turbofan engine intake at varying shaft speeds, in: 7th AIAA/CEAS Aeroacoustics Conference and Exhibit, American Institute of Aeronautics and Astronautics, 2001. doi:10.2514/6.2001-2181.

[19] D. Blacodon, Acoustic spinning-mode analysis by an iterative threshold method, Journal of Aircraft 32 (2) (1995) 377–384. doi:10.2514/3.46726.

[20] P. Sijtsma, J. Zillmann, In-duct and far-field mode detection techniques for engine exhaust noise measurements, Tech. Rep. NLR-TP-2007-347, National Aerospace Laboratory (NLR) (2007).

[21] M. Åbom, Modal decomposition in ducts based on transfer function measurements between microphone pairs, Journal of Sound and Vibration 135 (1) (1989) 95 – 114.

[22] S. Sack, M. Åbom, G. Efraimsson, On acoustic multi-port characterisation including higher order modes, Acta Acustica united with Acustica 102 (5) (2016) 834–850. doi:10.3813/aaa.918998.

[23] B. Lowrie, B. Tester, C. Morfey, Far-field methods of duct mode detection for broad-band noise sources, in: 4th Aeroacoustics Conference, American Institute of Aeronautics and Astronautics, 1977. doi:10.2514/6.1977-1331.

[24] B. Tester, A. Cargill, B. Barry, Fan noise duct-mode detection in the far-field - simulation, measurement and analysis, in: 5th Aeroacoustics Conference, American Institute of Aeronautics and Astronautics, 1979. doi:10.2514/6.1979-580.

[25] S. Lewy, H. Gounet, Experimental study of the acoustic spinning modes generated by a helicopter turboshaft engine, in: ICAS-92-1.5.1, 18th Congress of the International Council of the Aeronautical Sciences, Beijing, China, Vol. 1, 1992, pp. 898–906.

[26] F. Farassat, M. Myers, A study of wave propagation in a duct and mode radiation, in: Aeroacoustics Conference, American Institute of Aeronautics and Astronautics, 1996. doi:10.2514/6.1996-1677.

[27] F. Farassat, D. M. Nark, R. H. Thomas, The detection of radiated modes from ducted fan engines, in: 7th AIAA/CEAS Aeroacoustics Conference, Maastricht, The Netherlands, 2001, no. 2138, 2001.

[28] R. Thomas, F. Farassat, L. Clark, C. Gerhold, J. Kelly, L. Becker, A mode detection method using the azimuthal directivity of a turbofan model, in: 5th AIAA/CEAS Aeroacoustics Conference and Exhibit, American Institute of Aeronautics and Astronautics, 1999. doi:10.2514/6.1999-1954.

[29] J. Lan, J. Premo, D. Sutliff, Inlet mode measurements with an inflow control device microphone array, in: 8th AIAA/CEAS Aeroacoustics Conference, American Institute of Aeronautics and Astronautics, 2002. doi:10.2514/6.2002-2563.

[30] S. Lewy, Inverse method predicting spinning modes radiated by a ducted fan from free-field measurements, The Journal of the Acoustical Society of America 117 (2) (2005) 744–750.

[31] S. Lewy, Numerical inverse method predicting acoustic spinning modes radiated by a ducted fan from free-field test data, The Journal of the Acoustical Society of America 124 (1) (2008) 247–256. doi:10.1121/1.2931952.

[32] D. Venditti, O. Mehdizadeh, N. Joshi, A. Ali, Turbofan duct-mode identification using farfield noise measurements and numerical predictions, in: 12th AIAA/CEAS Aeroacoustics Conference (27th AIAA Aeroacoustics Conference), American Institute of Aeronautics and Astronautics, 2006. doi:10.2514/6.2006-2641.

[33] F. Castres, P. Joseph, J. Astley, Mode detection in turbofan inlets from acoustic pressure measurements in the radiated field, in: 10th AAIA/CEAS Aeroacoustics Conference, American Institute of Aeronautics and Astronautics, 2004, volume: 2004-2953.

[34] F. O. Castres, P. F. Joseph, Experimental investigation of an inversion technique for the determination of broadband duct mode amplitudes by the use of near-field sensor arrays, The Journal of the Acoustical Society of America 122 (2) (2007) 848–859.

[35] F. O. Castres, P. F. Joseph, Mode detection in turbofan inlets from near field sensor arrays, The Journal of the Acoustical Society of America 121 (2) (2007) 796–807.

[36] S. Fauqueux, R. Davy, Modal deconvolution method in a finite circular duct, using flush-mounted microphones, in: 2018 AIAA/CEAS Aeroacoustics Conference, American Institute of Aeronautics and Astronautics, 2018. doi:10.2514/6.2018-3927.

[37] P. Sijtsma, H. Brouwer, Deconvolution of azimuthal mode detection measurements, Journal of Sound and Vibration 422 (2018) 1–14. doi:10.1016/j.jsv.2018.02.029.

[38] M. Pestana, A. Pereira, E. Salze, J. Thisse, M. Sanjosé, E. Jondeau, P. Souchotte, M. Roger, S. Moreau, J. Regnard, M. Gruber, Aeroacoustics of an axial ducted low mach-number stage: numerical and experimental investigation, in: Proceedings of the 23rd AIAA/CEAS Aeroacoustics Conference, no. No. 2017-3215, 2017.

[39] T. Suzuki, B. J. Day, Comparative study on mode-identification algorithms using a phased-array system in a rectangular duct, Journal of Sound and Vibration 347 (2015) 27–45. doi:10.1016/j.jsv.2013.06.027.

[40] M. Behn, R. Kisler, U. Tapken, Efficient azimuthal mode analysis using compressed sensing, in: Proceedings of the 22nd AIAA/CEAS Aeroacoustics Conference, Lyon, France, no. No. 2016-3038, 2016.

[41] H. Bu, W. Yu, P.-W. Kwan, X. Huang, Wind-tunnel investigation on the compressive-sensing technique for aeroengine fan noise detection, AIAA Journal 56 (9) (2018) 3536–3546. doi:10.2514/1.j057261.

[42] X. Huang, A tutorial example of duct acoustics mode detections with machine-learning-based compressive sensing, The Journal of the Acoustical Society of America 146 (4) (2019) EL342–EL346. doi:10.1121/1.5128399.

[43] S. Sack, M. Åbom, Acoustic plane-wave decomposition by means of multilayer perceptron neural networks, Journal of Sound and Vibration 486 (2020) 115518. doi:10.1016/j.jsv.2020.115518.

[44] T. F. Brooks, W. M. Humphreys, A deconvolution approach for the mapping of acoustic sources (DAMAS) determined from phased microphone arrays, Journal of Sound and Vibration 294 (4-5) (2006) 856 – 879.

[45] M. Grant, S. Boyd, CVX: Matlab software for disciplined convex programming, version 2.1, http://cvxr.com/cvx (Mar. 2014).

[46] M. Munjal, Acoustics of ducts and mufflers with application to exhaust and ventilation system design, Wiley, 1987.

[47] Q. Leclère, A. Pereira, C. Bailly, J. Antoni, C. Picard, A unified formalism for acoustic imaging based on microphone array measurements, International Journal of Aeroacoustics 16 (4-5) (2017) 431–456. doi:10.1177/1475472X17718883.

[48] R. Merino-Martínez, P. Sijtsma, M. Snellen, T. Ahlefeldt, J. Antoni, C. J. Bahr, D. Blacodon, D. Ernst, A. Finez, S. Funke, T. F. Geyer, S. Haxter, G. Herold, X. Huang, W. M. Humphreys, Q. Leclère, A. Malgoezar, U. Michel, T. Padois, A. Pereira, C. Picard, E. Sarradj, H. Siller, D. G. Simons, C. Spehr, A review of acoustic imaging methods using phased microphone arrays, CEAS Aeronautical Journal 10 (1) (2019) 197–230.

[49] P. Sijtsma, Experimental techniques for identification and characterisation of noise sources,, in: Advances in Aeroacoustics and Applications, VKI Lecture Series, 5:15–19, 2004.

[50] C. J. Bahr, W. M. Humphreys, D. Ernst, T. Ahlefeldt, C. Spehr, A. Pereira, Q. Leclère, C. Picard, R. Porteous, D. Moreau, J. R. Fischer, C. J. Doolan, A comparison of microphone phased array methods applied to the study of airframe noise in wind tunnel testing, in: 23rd AIAA/CEAS Aeroacoustics Conference, American Institute of Aeronautics and Astronautics, 2017.

[51] J. Antoni, A bayesian approach to sound source reconstruction: Optimal basis, regularization, and focusing, The Journal of the Acoustical Society of America 131 (4) (2012) 2873–2890.

[52] N. Chu, A. Mohammad-Djafari, J. Picheral, Robust bayesian super-resolution approach via sparsity enforcing a priori for near-field aeroacoustic source imaging, Journal of Sound and Vibration http://dx.doi.org/10.1016/j.jsv.2013.02.037i (0) (2013).

[53] R. Roncen, F. Méry, E. Piot, Bayesian inference for modal identification in ducts with a shear flow, The Journal of the Acoustical Society of America 146 (4) (2019) 2645–2654. doi:10.1121/1.5130195.

[54] P. A. Nelson, S. H. Yoon, Estimation of acoustic source strength by inverse methods: Part i, conditioning of the inverse problem, Journal of

Sound and Vibration 233 (4) (2000) 639 – 664.
[55] Q. Leclère, Acoustic imaging using under-determined inverse approaches: Frequency limitations and optimal regularization, Journal of Sound and Vibration 321 (3-5) (2009) 605 – 619.
[56] A. Pereira, J. Antoni, Q. Leclère, Empirical bayesian regularization of the inverse acoustic problem, Applied Acoustics 97 (2015) 11 – 29.
[57] J. Antoni, T. L. Magueresse, Q. Leclère, P. Simard, Sparse acoustical holography from iterated bayesian focusing, Journal of Sound and Vibration 446 (2019) 289–325.
[58] D. R. Hunter, K. Lange, A tutorial on MM algorithms, The American Statistician 58 (1) (2004) 30–37. doi:https://doi.org/10.1198/0003130042836.
[59] I. Gorodnitsky, B. Rao, Sparse signal reconstruction from limited data using FOCUSS: a re-weighted minimum norm algorithm, IEEE Transactions on Signal Processing 45 (3) (1997) 600–616. doi:10.1109/78.558475.
[60] I. Daubechies, R. DeVore, M. Fornasier, C. S. Güntürk, Iteratively reweighted least squares minimization for sparse recovery, Communications on Pure and Applied Mathematics 63 (1) (2010) 1–38.
[61] G. H. Golub, M. Heath, G. Wahba, Generalized cross-validation as a method for choosing a good ridge parameter, Technometrics 21 (2) (1979) 215–223.
[62] P. C. Hansen, D. P. O'Leary, The use of the L-curve in the regularization of discrete ill-posed problems, SIAM J. Sci. Comput. 14 (1993) 1487–1503.
[63] S. H. Yoon, P. A. Nelson, Estimation of acoustic source strength by inverse methods: Part ii, experimental investigation of methods for choosing regularization parameters, Journal of Sound and Vibration 233 (4) (2000) 665 – 701.
[64] Y. Kim, P. A. Nelson, Optimal regularisation for acoustic source reconstruction by inverse methods, Journal of Sound and Vibration 275 (3-5) (2004) 463 – 487.
[65] M. Behn, U. Tapken, Investigation of sound generation and transmission effects through the ACAT1 fan stage using compressed sensing-based mode analysis, in: 25th AIAA/CEAS Aeroacoustics Conference, American Institute of Aeronautics and Astronautics, 2019.
[66] U. Tapken, M. Behn, M. Spitalny, B. Pardowitz, Radial mode breakdown of the ACAT1 fan broadband noise generation in the bypass duct using a sparse sensor array, in: 25th AIAA/CEAS Aeroacoustics Conference, American Institute of Aeronautics and Astronautics, 2019.
[67] R. Meyer, S. Hakanson, W. Hage, L. Enghardt, Instantaneous flow field measurements in the interstage section between a fan and the outlet guiding vanes at different axial positions, in: ETC13, Lausanne, Switzerland, 2019.
[68] V. M. Patel, G. R. Easley, D. M. Healy, R. Chellappa, Compressed synthetic aperture radar, IEEE Journal of Selected Topics in Signal Processing 4 (2) (2010) 244–254. doi:10.1109/JSTSP.2009.2039181.
[69] J. Antoni, Cyclostationarity by examples, Mechanical Systems and Signal Processing 23 (4) (2009) 987 – 1036.
[70] S. Lewy, S. Canard-Caruana, J. Julliard, Experimental study of noise sources and acoustic propagation in a turbofan model, AIAA Paper 90-3950, October, 1990. doi:10.2514/6.1990-3950.
[71] R. Blázquez-Navarro, R. Corral, Prediction of fan acoustic blockage on fan/outlet guide vane broadband interaction noise using frequency domain linearised navier–stokes solvers, Journal of Sound and Vibration 500 (2021) 116033. doi:https://doi.org/10.1016/j.jsv.2021.116033.
[72] C. Brandstetter, B. Paoletti, X. Ottavy, Compressible Modal Instability Onset in an Aerodynamically Mistuned Transonic Fan, Journal of Turbomachinery 141 (3), 031004 (01 2019).
[73] U. W. Ganz, P. D. Joppa, T. J. Patten, D. F. Scharpf, Boeing 18-inch fan rig broadband noise test, Tech. Rep. CR-1998-208704, NASA (1998).
[74] C. Lowis, P. Joseph, A. Kempton, Estimation of the far-field directivity of broadband aeroengine fan noise using an in-duct axial microphone array, Journal of Sound and Vibration 329 (19) (2010) 3940 – 3957.
[75] B. J. Tester, Y. Özyörük, Predicting far-field broadband noise levels from in-duct phased array measurements, in: 20th AIAA/CEAS Aeroacoustics Conference, American Institute of Aeronautics and Astronautics, 2014.
[76] R. P. Dougherty, R. Bozak, Two-dimensional modal beamforming in wavenumber space for duct acoustics, in: 2018 AIAA/CEAS Aeroacoustics Conference, American Institute of Aeronautics and Astronautics, 2018.
[77] E. Salze, E. Jondeau, A. Pereira, S. L. Prigent, C. Bailly, A new MEMS microphone array for the wavenumber analysis of wall-pressure fluctuations: application to the modal investigation of a ducted low-mach number stage, in: 25th AIAA/CEAS Aeroacoustics Conference, American Institute of Aeronautics and Astronautics, 2019.
[78] C. Morfey, Sound transmission and generation in ducts with flow, Journal of Sound and Vibration 14 (1) (1971) 37–55.
[79] P. Joseph, C. Morfey, C. Lowis, Multi-mode sound transmission in ducts with flow, Journal of Sound and Vibration 264 (3) (2003) 523–544.
[80] F. Bowman, Introduction to Bessel Functions, Dover Books on Mathematics, Dover Publications, 1958.